Heliyon 8 (2022) e10651

Contents lists available at ScienceDirect

Heliyon

journal homepage: www.cell.com/heliyon

Review article

Robocasting of advanced ceramics: ink optimization and protocol to predict the printing parameters - A review

Soukaina Lamnini [a,b], Hamada Elsayed [c,d], Yazid Lakhdar [e], Francesco Baino [a,*], Federico Smeacetto [a], Enrico Bernardo [c]

[a] Institute of Materials Physics and Engineering, Department of Applied Science and Technology, Politecnico di Torino, 10129 Torino, Italy
[b] Materials Science, Energy & Nano engineering, MSN Department, University Mohammed VI Polytechnic Benguerir, Morocco
[c] Department of Industrial Engineering, University of Padova, 35100 Padova, Italy
[d] Ceramics Department, National Research Centre, El-Bohous Street, 12622 Cairo, Egypt
[e] School of Metallurgy and Materials, University of Birmingham, Edgbaston, Birmingham, B15 2TT, UK

ARTICLE INFO

Keywords:
Robocasting
Glass
Ceramics
Feedstock features
Printing parameters

ABSTRACT

Direct-Ink-Writing (or robocasting) is a subset of extrusion-based additive manufacturing techniques that has grown significantly in recent years to design simple to complex ceramic structures. Robocasting, relies on the use of high-concentration powder pastes, also known as inks. A successful optimization of ink rheology and formulation constitutes the major key factor to ensure printability for the fabrication of self-supporting ceramic structures with a very precise dimensional resolution. However, to date achieving a real balance between a comprehensive optimization of ink rheology and the determination of a relevant protocol to predict the printing parameters for a given ink is still relatively scarce and has been not yet standardized in the literature.

The current review reports, in its first part, a detailed survey of recent studies on how ink constituents and composition affect the direct-ink-writing of ceramic parts, taking into account innovative ceramic-based-inks formulations and processing techniques. Precisely, the review elaborates the major factors influencing on ink rheology and printability, specifically binder type, particle physical features (size, morphology and density) and ceramic feedstock content.

In the second part, this review suggests a standardized guideline to effectively adapt a suitable setting of the printing parameters, such as printing speed and pressure, printing substrate, strut spacing, layer height, nozzle diameter in function of ink intrinsic rheology.

1. Introduction

Additive manufacturing (AM), which is also known as three-dimensional (3D) printing, refers to a set of fabrication procedures that enable the creation of objects by adding or joining the material rather than removing or cutting away the material, like in the case of subtractive manufacturing. This gives a potential role of additive manufacturing in reducing the wastage of raw materials, in addition to its uniqueness in fabricating products with complex shapes, which makes such strategies suitable for various and wide range of engineering applications [1, 2].

Additive manufacturing techniques allow the construction of objects point-by-point, line-by-line or layer-by-layer following Computer-Aided Designs (CAD) as virtual templates. Depending on the nature of feedstock which is considered as the raw material before the printing process, the additive manufacturing techniques, especially for ceramic materials, can be classified into powder-based 3D printing (i.e. binder jetting, powder-based three-dimensional printing (3DP), selective laser melting (SLM) and selective laser sintering (SLS)), liquid, suspension and slurry-based 3D printing (i.e. stereolithography (SL), digital light processing (DLP), two-photon polymerisation (TPP), inkjet printing (IJP), direct ink writing (DIW), slurry-based 3DP (S-3DP) and slurry-based SLS (S-SLS)), and solid-based 3D printing (i.e. laminated object manufacturing (LOM) and fused deposition modelling (FDM, also known as fused filament fabrication, FFF)) [3, 4, 5, 6].

Taking into account how the material is deposited, additive manufacturing technologies can be divided into direct and indirect 3D printing techniques. The indirect 3D printing techniques include the deposition of a layer and, afterwards, the object shape is formed on this

* Corresponding author.
E-mail address: francesco.baino@polito.it (F. Baino).

https://doi.org/10.1016/j.heliyon.2022.e10651
Received 22 August 2022; Received in revised form 7 September 2022; Accepted 9 September 2022

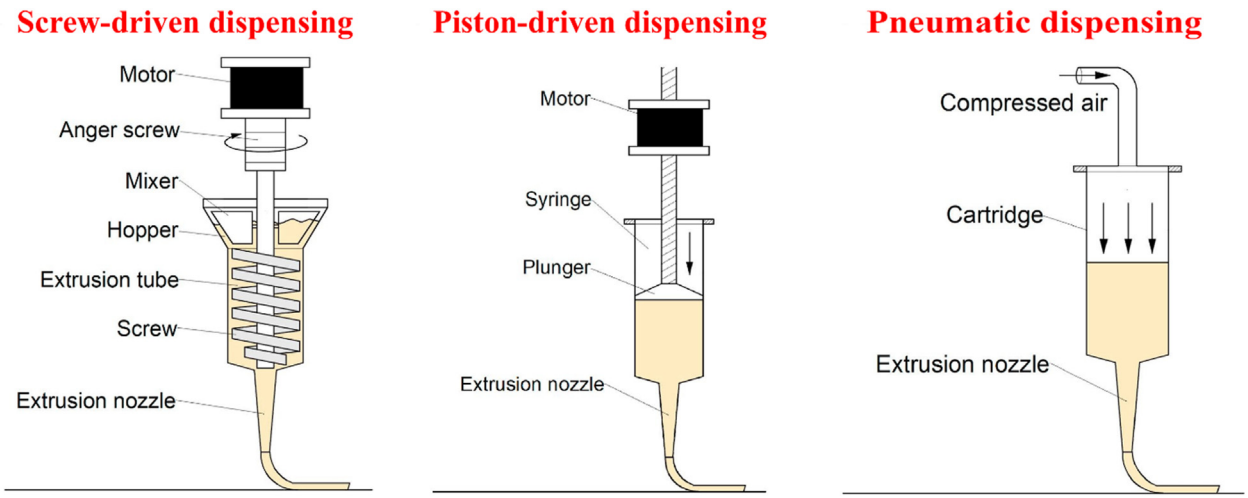

Figure 1. Representation of different apparatus configurations used for extruding the high-solid-loading viscous pastes, where the mechanical displacement in screw-driven, the rotation in piston-dispensing and the air pressure in pneumatic dispensing, respectively, deliver the driving force to ensure a continuous flow of the ink through the nozzle [9].

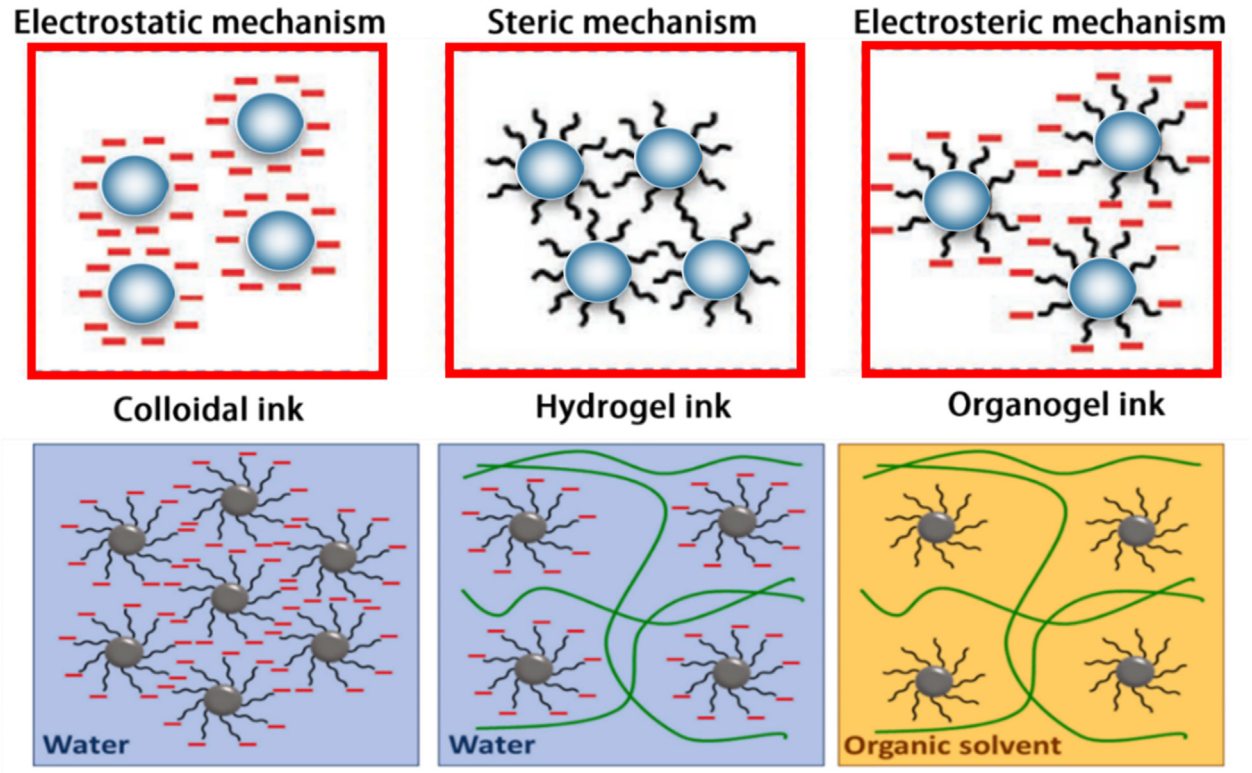

Figure 2. Schematic diagram illustrating the three main mechanisms for particle stabilisation: steric and electrostatic interactions are represented with black lines and negative red charges respectively. Colloidal inks involve an electro-steric stabilization mechanism, which gives rise to polyelectrolyte complexes. The green lines represent the polymer chains within gel-embedded inks. Adapted with permission from [18].

layer; then, the process is repeated until the end of the printing process. As a result, the printed shape is supported by excess material to be removed, in the end, to extract the shaped part. Powder-based printing, selective laser sintering and melting, stereolithography, slurry-based 3DP, and slurry-based SLS are considered indirect printing additive manufacturing techniques. On the other hand, for direct 3D printing, the materials could be directly deposited in the selective sites developing the required structure of the target object. The direct 3D printing techniques include inkjet, direct ink writing, fused deposition modelling, and filament extrusion 3D printing [3, 4, 5, 6].

Direct Ink Writing (DIW), also known as "robocasting", is an extrusion-based additive manufacturing process that involves the use of highly concentrated powder suspensions (also known as inks). The inks are extruded in the form of filaments (whereas inks for inkjet printing are distributed in droplets) through narrow nozzles under external pressure, employing a computer-controlled model to direct the printing head layer-by-layer only in the positions that give the final shape of the desired object [7, 8]. A schematic diagram of DIW is reported in Figure 1, showing the extrusion mechanism of the inks through thin nozzles with different kinds of extrusion setups [9, 10].

Table 1. Powder-additive systems used for robocasting of ceramic parts.

Feedstock	Additives and solvents	Solid loading (vol.%)	Mixing steps	Density/porosity	Applications	De-binding and sintering treatment	Ref.
Bioactive glass	- Pluronic F-127 - DI water	35	**Vortex mixer (5 mixing -cooling cycles):** -1 min at 2500 rpm. - 1min cooling.	-	Scaffolds for bone regeneration.	**De-binding:** 200 °C, 400 °C, and 500 °C for 30 min each in air. **Sintering:** 600 °C for 1 h in air.	[52]
Bioactive glass	-CMC-250 - DI water	45	**Planetary centrifugal mixer:** 20 min in total.	**Porosity:** 20 vol%.	Scaffolds for cancellous bone.	**De-binding**: 400 °C for 1 h in air. **Sintering**: up to 1200 °C for 1 h in air.	[45]
Al_2O_3	-Darvan C-N -Bermocoll - PEI -DI water	50	**Ball milling:** 48 h in total.	**Residual porosity:** 8.9 ± 2.6 vol %.	Ceramic scaffolds with anisotropic microstructure.	**Direct sintering:** 1600 °C for 1 h in air.	[64]
Al_2O_3	-Pluronic F-127 - DI water	40	**Planetary centrifugal mixer (mixing/cooling cycles):** 1. mixing at 2000 rpm for 1 min. 2. cooling at 4 °C for 24 h. 3. two mixing cycles at 2000 rpm for 1 min and cooling to 0 °C. 4. cooling and mixing for 2 min at 2200 rpm.	**Relative density:** 97 ± 1% TD.	Complex ceramic parts with low porosity and high strength.	**De-binding:** 600 °C for 2 h in air. **Sintering:** PSPS at 1550 °C for 1h in air.	[66]
YSZ	- Polyelectrolyte dispersant (Dolapix) - Hydroxypropyl methylcellulose (HPMC) - PEI - DI water	48	**Planetary centrifugal mixer**	**Density:** 6.04 ± 0.06 g cm^{-3}. **Micro porosity:** ~0.2 vol%. **Macro porosity:** 69.84 ± 0.01vol %.	Load bearing implants with osseointegration and bone bonding ability.	**De-binding:** 600 °C, with a soaking time of 1 h. **Sintering:** 1450 °C for 1 h in air.	[60]
B_4C	- PEI - Deionised water - Stearic acid - Pluronic F-127 (10–17 wt%)	46 to 50	**Planetary centrifugal mixer:** - 2000 rpm for 1 min, once at the beginning of each powder batch addition, and then twice with a 15 s cool-off break.	**Relative density:** 94–97 % TD.	Manufacturing monolithic B_4C components for industrial applications: abrasive tools, sandblasting nozzles.	**De-binding:** 500 °C in argon. **Sintering:** high-temperature vacuum furnace under argon gas up to 2275 °C for 1 h.	[56, 67]
CEZ-12 Ceria-stabilized zirconia powder	- Pluronic F127 - DARVAN - DI water	36	**Planetary centrifugal mixer:** 1800 rpm.	**Porosity:** 85 vol%.	Complex porous structures for various applications in bio-medical or energy storage fields.	**De-binding:** 350 °C, 600 °C for a dwell of 2 h at 600 °C. **Sintering:** 800 °C, 1000 °C, 1250 °C dwell of two hours at 1250 °C.	[61]
Hydroxyapatite (HA, 20V %)/-tricalcium phosphate (TCP, 80V%)	-Pluronic F127 - DI water - Polymeric beads	30 (2 vol, Polymeric beads)	**Mixing in a jar.**	**Relative density:** 60 ± 1. **Porosity of macropores:** 40 ± 1 vol%.	HA/-TCP scaffolds for bone substitution.	**De-binding:** 550 °C for 2 h. **Sintering:** 1100 °C for 4 h.	[53]
Si_2N_2O	-Tetraethyleneglycol - Dimethylether - DI water -PVA -(NH4) H_2PO4	21.17	**Mechanical stirring:** 1h.	**Density:** 1.14 ± 0.05 g/cm^3. **Apparent porosity:** 52.79 ± 1.83 vol%.	Highly porous structural/ functional ceramic parts.	**De-binding:** 300 °C for 2 in air, 600 °C for 2 h in air. **Sintering:** 1650 °C for 2 h under 1atm N_2.	[68]

(*continued on next page*)

Table 1 (*continued*)

Feedstock	Additives and solvents	Solid loading (vol.%)	Mixing steps	Density/porosity	Applications	De-binding and sintering treatment	Ref.
Si_3N_4	- PEI - DI water	35	**Planetary centrifugal mixer.**	**Density**: 3.230.01 g/cm^3.	Orthopaedic and dental surgery.	**De-binding:** 300 °C and 600 °C for 2h. **Sintering:** hot isostatic pressing for 2 h at ~1700 °C in N_2.	[69]
SiC- Al_2O_3- Y_2O_3	- H-PEI - L-PEI - Methylcellulose - APA - DI water	44	**Planetary centrifugal mixer:** - 1 min after each powder addition. - Homogenization by high shear Mixing at the end.	**Relative density**: 97% TD.	Geometrically complex, three-dimensional (3-D) structures of SiC for structural and functional applications.	**De-binding:** 600 °C for 2 h in air. **Sintering:** SPS at 1700 °C for 5 min in argon atm.	[31]
B_4C	- Polyelectrolyte dispersant. - DI water - Methylcellulose - PEI	40	**Agitation cycles:** - 10 min at 700 rpm, 800 rpm, 1000 rpm. - 2 min at 1200 rpm. - 7 min at 700 rpm.	**Relative density:** 90 ± 3%TD.	Geometrically complex B_4C for vehicle armour components and tribo-components such as: nozzles for blasting and waterjet cutting, cutting tools and dies, and other wear resistant parts.	**Direct sintering:** PSPS at 2100 °C for 5 min under vacuum.	[55]

Compared to conventional methods, the DIW technique provides many advantages, including the fabrication of complex geometries with high precision in the form of both dense and porous parts. Compared to other AM techniques, DIW is faster and more affordable in terms of the cost, open source of printing units, versatility and possibility of printing various materials such as ceramics, polymers, metals, and composites. Further advantages of the DIW technique reside in the possibility to fabricate nano- and micro-sized materials in small amounts, which could be considered a critical issue and problematic to handle in powder-bed printing. Therefore, it is an eco-friendly technique, particularly when the printing process is performed in the air in an ambient environment setup [4, 5, 6, 7, 11, 12].

Ink rheology constitutes a major factor to print self-supporting parts in DIW. The inks should possess suitable rheological properties, displaying a shear-thinning behaviour during extrusion (i.e., printing process) and consistency after deposition. The addition of additives (such as appropriate dispersants, viscosifiers, plasticisers, and thickeners) is important for viscosity adjustment and particle dispersion while the solid loading volume fraction affects the viscoelastic properties: storage modulus (G′) and loss modulus (G) [13, 14]. The shear-thinning behaviour allows the ink to flow through micro-nozzles, due to the viscosity decrease of several orders of magnitude as a result of an increase of shear rate upon the application of an external force on the ink. After the deposition of the ink, the shear rate suddenly decreases and the viscosity rapidly increases to high values, thereby allowing the filament to keep its shape and providing adequate shape retention. In addition, the ink behaviour changes from the pseudoplastic to dilatant due to a slight drying and solidification upon evaporation of the solvent. Thus, after extrusion from small nozzles, the high-solid-loading inks with the above-mentioned rheological properties are capable of keeping their physical integrity and supporting their weight without deformation and bending (which is key to span large spacing in case of printing porous lattices), eventually yielding effective fabrication of the printed part layer-by-layer [15, 16, 17, 18, 19].

Inks designed with high solid content and viscoelastic properties enable shape retention of the extruded filaments, thus leading to the fabrication of freestanding, suspended structures with different spacing lines, which is not achievable with other AM techniques such as powder bed printing [13, 15, 20, 21]. High-solid-loading viscous pastes are suitable for DIW to allow the printing of 3D parts with high green density after extrusion through thin nozzles [1]. Thereby, this leads to high-density ceramic, glass, and glass-ceramic parts with better mechanical properties as compared to powder bed printing after the heat-treatment of sintering at high temperatures.

Major aspects influencing the rheological behaviour of the starting suspensions include solid loading, type and concentration of additives, size distribution and density of particles as well as the relevant preparation procedure that should result in uniform interfacial solid/liquid interactions. In addition, the effective destruction of hard agglomerates is of great importance as it highly influences the suspensions flowability, homogeneity and sintering ability. A homogenous texture free of air bubbles enables ensuring the continuity of the build pattern and full densification of the green bodies at relatively low sintering temperatures [22, 23]. It is worth noting that the rheological properties required for robocasting differ from one material to another concerning the specific application it is designed for [24].

The choice of solvents with a controlled evaporation rate, which allows creating inks based on the aqueous and nonaqueous mixed systems, is considered at the top of the challenges of the DIW technique. A wise selection is key to ensure continuous flowing and extrusion of the ink through small nozzles without clogging the nozzle during printing and creating defects in the printed parts.

In addition, applying a uniform and slow drying process for the as-printed ceramic products is advisable to prevent further shrinkage due to fast drying rate and the formation of residual drying cracks [25, 26, 27, 28, 29, 30]. Typical convection heaters, desiccators, microwaves, heat or

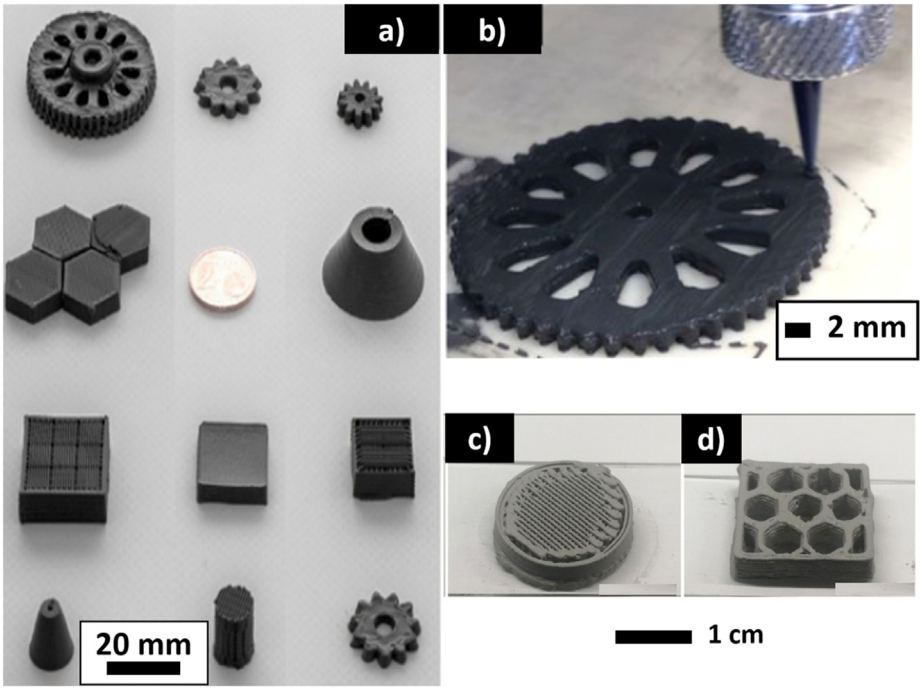

Figure 3. Optical images of geometrically complex B_4C printed ceramic parts using robocasting: a) green and dried B_4C parts shaped by robocasting, b) in situ image of complex circular gear during printing adapted with permission from [55]. Optical images of Si_3N_4 printed structures using robocasting: c) cellular structure and d) honeycomb structure adapted with permission from [65].

custom-built enclosures can be used to ensure homogenous drying process which depends on local conditions such as humidity (65–80%) or the ambient temperature [31, 32, 33, 34]. This is to highlight that a quantified setting of all these general criteria as well as the choice of a relevant protocol to predict the optimal printing parameters from the software is greatly influencing the printing outcome. More specifically, printing and travel speeds, retraction distance and speed, layer height and filling constitute the cornerstone to successfully robocast a given ink and

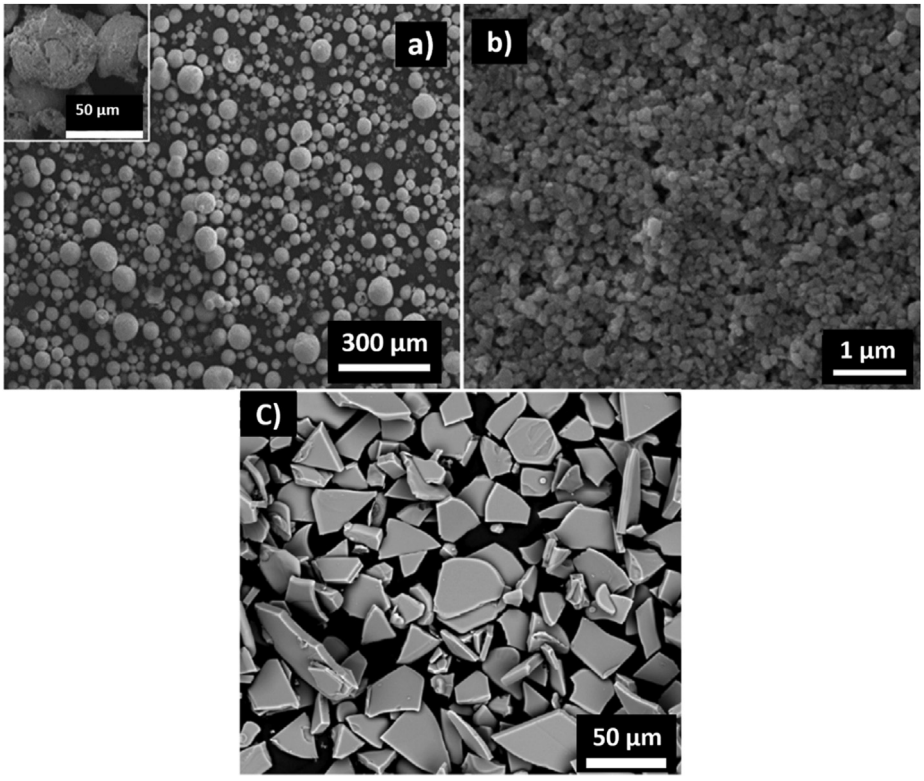

Figure 4. SEM micrographs showing powder morphology and size used for ink preparation: a) zirconia granules and b) zirconia particles derived from the crushed granules after planetary and rotational milling, c) silicon carbide platelets incorporated in aqueous silicon carbide paste designed for robocasting. Adapted with permission from [80] and [81] respectively.

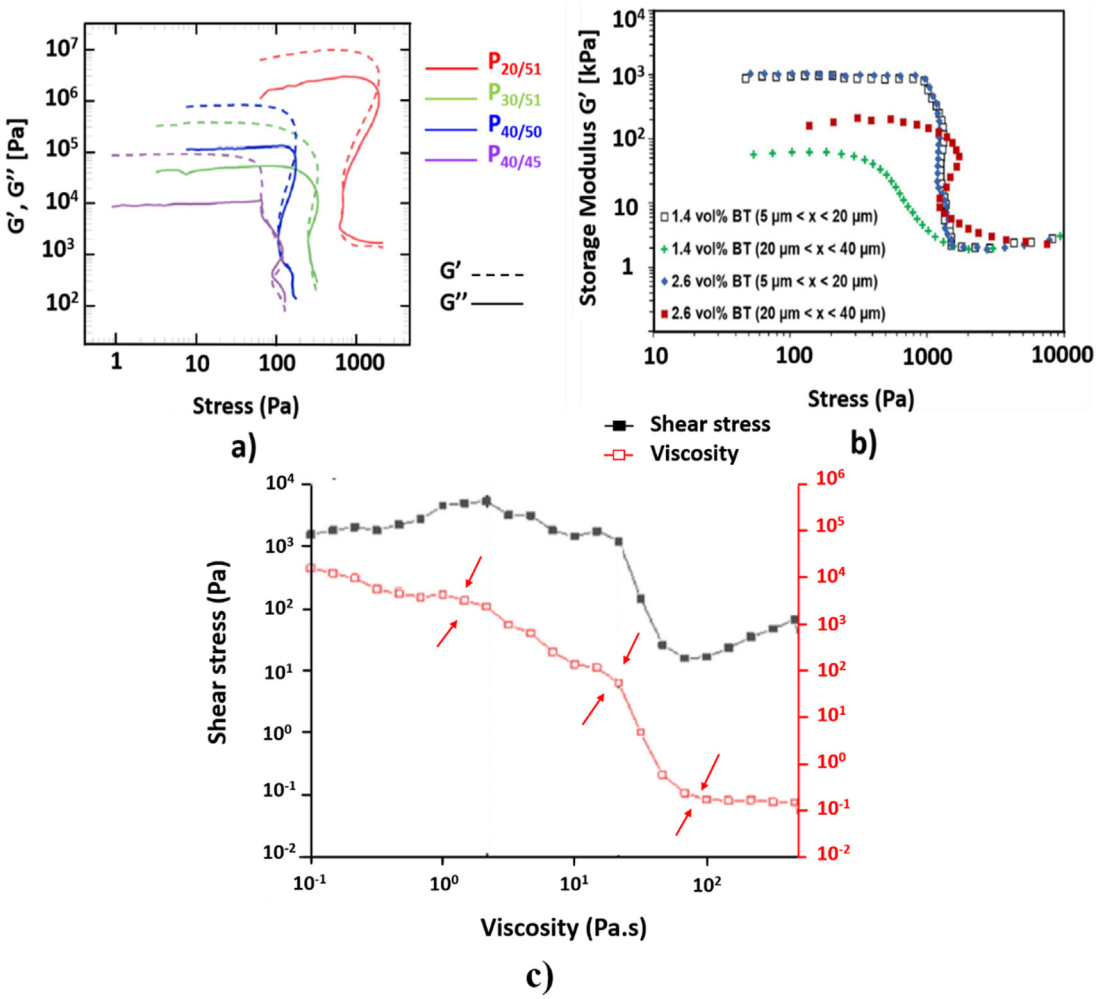

Figure 5. Amplitude-sweep curves showing the variation of storage modulus G′ and loss modulus G″ in function of stress for: a) pastes containing Al_2O_3 platelets at various content of 20, 30, 40 vol% in relation to the total ceramic content of 51, 50,45 vol% and b) paste containing 28 vol% of $BaTiO_3$ platelets at different sizes and amounts. c) Shear stress and viscosity curve showing the viscosity instability due to pastes produced from granules. a), b) and c) images are adapted with permission from [79, 83] and [80] respectively.

achieve a targeted resolution. On the other hand, the controlled de-binding stage and sintering phase are necessary to get final printed parts with specific physical, microstructural, and mechanical properties [35, 36, 37].

2. Optimization of ink formulation and sintering process for robocasting

One of the major challenges in robocasting concerns the preparation of suitable high-solid-loading ceramic pastes with a low concentration of additives while exhibiting pseudoplastic properties. Therefore, understanding the mutual interaction between additives and ceramic powders remains crucial to tune the rheological features of the ceramic suspensions and the structural properties after post-treatment. Aqueous inks for robocasting are in general formulated by a mixture of glass powder, water, and additives. The ceramic powder (>40.0 vol%) and organic additives (<3.0 vol%) should be carefully optimized to obtain a homogeneous suspension and minimize post-printing shrinkage [7, 17]. Appropriate inks for layer-wise deposition using robocasting are commonly loaded in a syringe to print dense or porous ceramics and composites.

In classical robocasting inks, the additives can be a mixture of dispersants, thickeners (binders), and coagulants. Dispersants are polymers adsorbed on the ceramic/glass particle surfaces to reduce interparticle friction and overcome van der Waals interparticle attractive forces between powders to produce a homogeneous structure which enables the printability of the paste by robocasting [13, 38]. There are three mechanisms to stabilize ceramic particles in a solution as shown in Figure 2, namely electrostatic, steric, or combined electro-steric strategies [39]. The stabilization of aqueous polyelectrolyte and polyelectrolyte complex inks involves electrostatic or electro-steric mechanisms. The electro-steric stabilization occurs with highly concentrated suspensions by adding polyelectrolyte species such as polyacrylate (PAA), poly(vinyl alcohol) (PVA), and polyethyleneimine (PEI) that contain ionizable functional (e.g. amine (-NH_2) or carboxylic (-COOH)) groups [17, 38, 40].

On the other hand, steric stabilization characterizes nonaqueous solvent-based ink where steric repulsion forces are induced by the adsorbed organic molecules to prevent agglomeration [39, 41].

The binder system is usually a multi-constituent polymer with high molecular weight used to induce flowability, increase the viscosity and act as a bonding agent joining the particles together until the final stages of de-binding. The optimization and the choice of the additive system (binder/plasticizer/thickener) is of great importance to allow the fast and effective burnout of additives through multi-stage thermal treatment while preventing the creation of cracks and internal flows within the final product microstructure [17, 42, 43].

Similarly, coagulants are special polymers acting as glues to provide resistance to the external forces and enhance the viscoelastic response [13].

Table 2. Powder features and rheological properties as key factors affecting the printability of different ceramic inks.

Feedstock	Particle size, S (μm)	Powder shape	Solid loading (vol%)	Viscosity at $0.1s^{-1}$ shear (Pa·s)	Yield stress, σ_y (Pa)	Storage Modulus, G′ (Pa)	Ref.
Lead-based perovskites/ $BaTiO_3$	bimodal distribution: $5 < S < 20$	platelet	28	-	1370	10^6	[83]
Lead-based perovskites/ $BaTiO_3$	bimodal distribution: $20 < S < 40$	platelet	28	-	1500	60×10^3	[83]
Al_2O_3–Y_2O_3	bimodal distribution: $S_{1average} = 0.15$ $S_{2average} = 1.0$	subrounded	42	10^3	10^3	10^6	[92]
$BaTiO_3$	bimodal distribution: $d_{50} = 1.2$	subrounded	52	3.5×10^4	694	10^7	[86]
$BaTiO_3$	bimodal distribution: $d_{50} = 1.2$	subrounded	50	2×10^4	142	10^6	[86]
Al_2O_3	bimodal distribution: $S_{sphere\ average} = 0.5$ $S_{platelet\ average} = 4.1$	**mixture of shapes**: sphere-and platelet	51 (20 vol% of alumina pellet)	-	633	10^7	[79]
Al_2O_3	bimodal distribution: $S_{sphere\ average} = 0.5$ $S_{platelet\ average} = 4.1$	**mixture of shapes**: sphere and platelet.	51 (30 vol% of alumina pellet)	-	265	10^6	[79]
ZnO	monomodal distribution: $S_{average} = 0.7$	irregular	48	6.53	11	2×10^4	[91]
3Y–ZrO_2	multimodal distribution: $S_{1average} = 0.8$ $S_{2average} = 3.9$ $S_{3average} = 18.9$ $S_{4average} = 52.6$	uniform solid spheres	42	10^4	1.98×10^3	3×10^5	[80]
3Y–ZrO_2	monomodal distribution: $S_{average} = 0.17$	uniform solid spheres	53	2×10^4	14.07×10^3	4×10^6	[80]

The printed green ceramic bodies obtained from solvent-based pastes need consolidation through post-printing treatments. In general, a few hours of drying are required to evaporate the solvent before de-binding (organic binder burnout), followed by a sintering process. Indeed, no thermal post-treatment should be carried out if the fabrication of polymer/ceramic composite structures is a goal. Adequate choice of additives, as well as their proportions, is a crucial step to tune the final product features since the de-binding of organic binders leaves little residues that reduce the mechanical and structural integrity [38].

The presence of many components (dispersants, thickeners and coagulants) in the colloidal suspension drastically influences the balance between the anionic and cationic forces that tend to change the pH and,

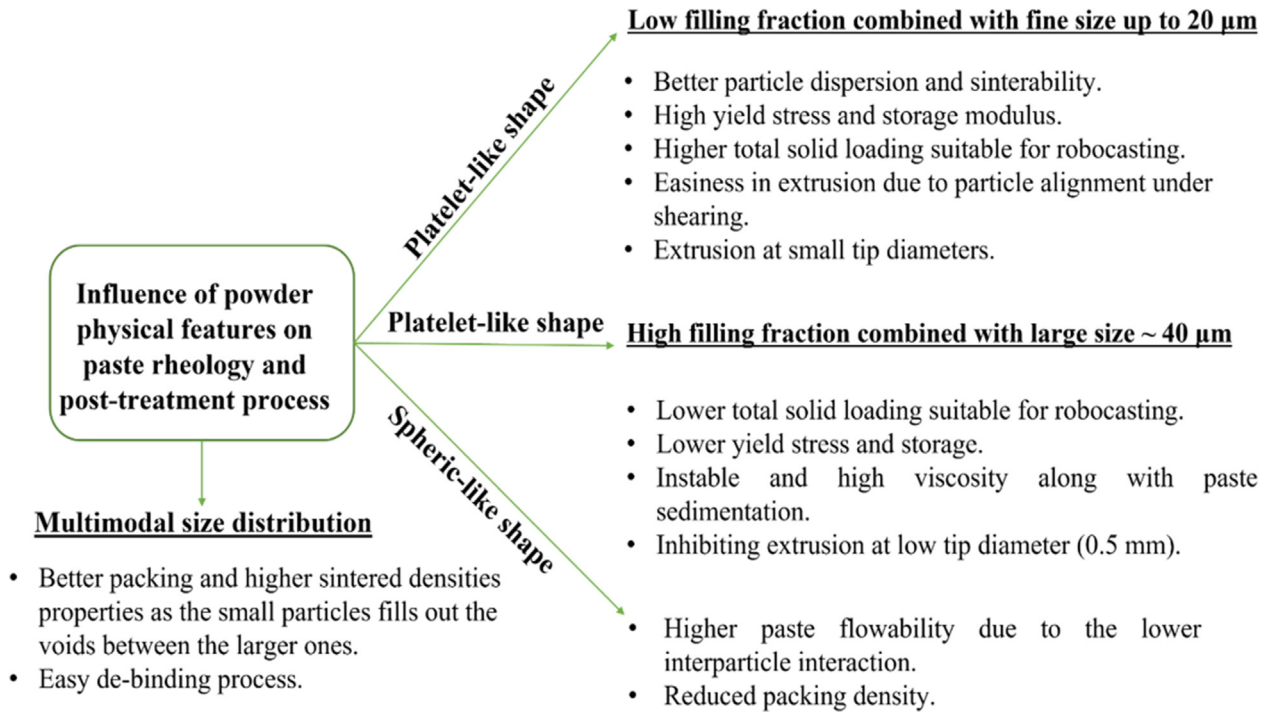

Figure 6. A schematic summarizing the influence of grain size, shape on paste rheology and post-treatment process.

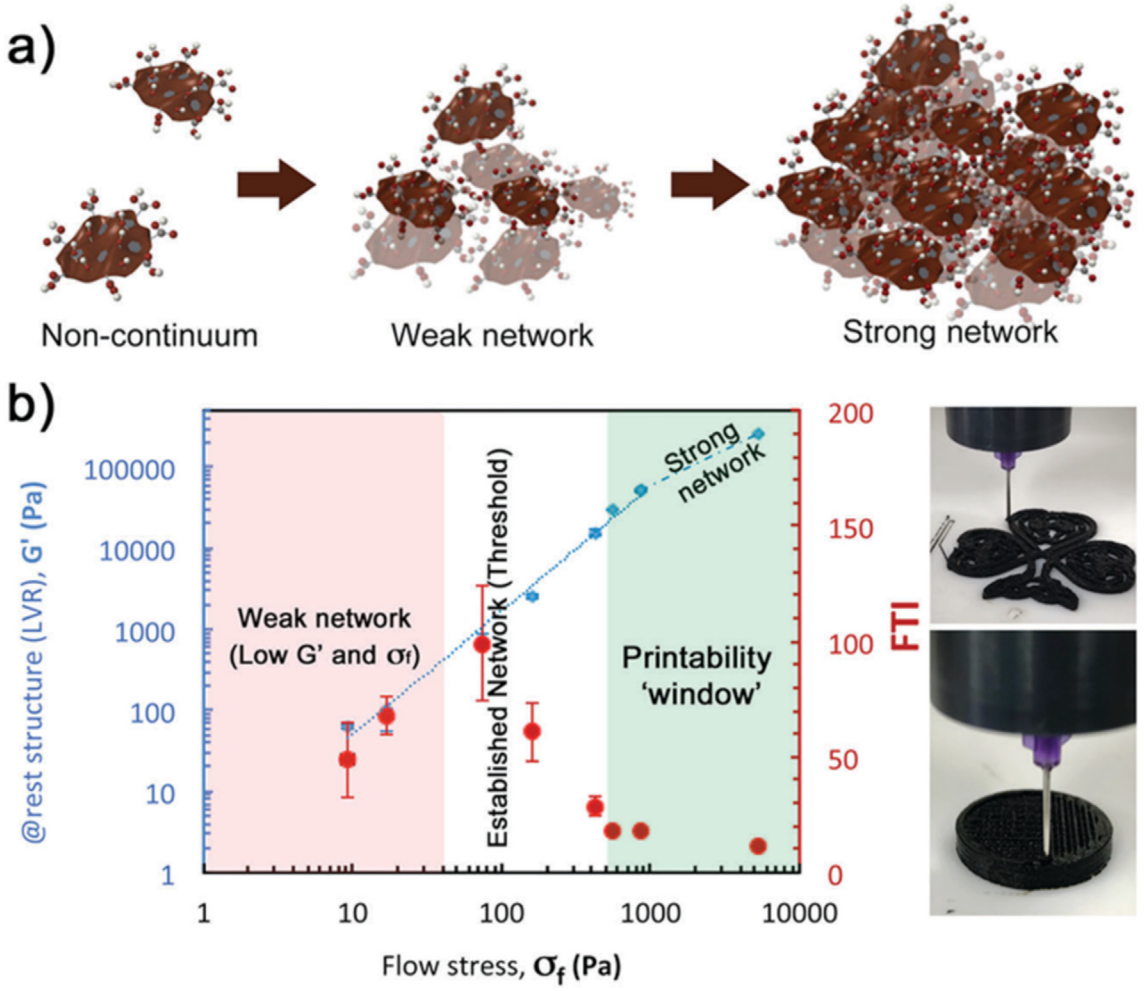

Figure 7. a) Colloidal particles in aqueous suspensions can form a non-continuous, weak, or strong network depending on the particle volume fraction. b) Printability map for GO suspensions including three key rheology parameters: at rest structure or network stiffness (G_{LVR}'), flow stress, σ_f (oscillation stress at the crossover point, when $G' = G''$), and flow transition index FTI (the ratio between the flow stress and the yield stress, σ_f/σ_y). The stiffness (G_{LVR}') of the GO networks increase as sf increases following a power relationship up to 2.8 vol%. The trend changes abruptly at 3 vol%. At concentrations below 0.8 vol% the network across flakes is weak, resulting in very small values of σ_f and G', in this range FTI values do not display a clear trend. From 0.8 vol%, considered as the 'network threshold', the FTI clearly decreases revealing the 'brittle' character of the networks. Printable concentrations, between 2 vol% and 3 vol%, exhibit an FTI value <20 with small uncertainties and a G'/σ_f ratio ≥20. Adapted with permission from [15].

hence, create a non-stable suspension [22, 42]. In fact, the fast solvent evaporation of the colloidal suspension in ambient conditions may cause both clogging during printing with fine nozzles in a low humidity setting and crack formation after printing. In order to mitigate such a problem, attention has been raised toward the use of gel-embedded suspensions (aqueous hydrogel-forming ink) or combined inks comprising both aqueous and non-volatile hydrophilic co-solvents [65]. The easy and fast processing of gel-embedded suspensions results in stable suspensions as the rheological properties depend on the gel properties rather than particle-particle interactions.

Gel-embedded suspensions based on carboxymethyl cellulose (CMC) [44, 45] and Pluronic F–127 [46,47], are the most usual choices in which a single multifunctional additive acts as a dispersant, plasticizer, and coagulant agent.

CMC is an important element in the paste formulation as it allows modulating the rheological properties – especially the flowability of the paste – by means of interactions with the surface of solid loading particles, being partially adsorbed onto them [48].

Eqtesadi et al. shed light on the importance of using high-molecular-weight CMC-250 rather than CMC-35 to tune the ink rheological properties for robocasting [44]. The comparative study on the two inks based on CMC- 250 and CMC-35 at fix solid loading up to 45 vol% of 45S5 Bioglass® powder demonstrated the benefit of CMC- 250 to induce a stronger thickening behaviour, particularly at low concentration (1 wt %). Furthermore, the longer CMC-250 chains at low concentration (1 wt %) enable optimal shape retention as the ink shows the highest elastic modulus along with relatively low viscosity (800–200 Pa s at 1–100 s^{-1} shear rates), which mainly dictates its flowability.

In the same context, Eqtesadi et al. [45] prepared scaffolds from 45S5 Bioglass® powders by robocasting using CMC as a single multifunctional additive. Ink formulation consisted of 1 wt.% CMC dissolved in deionized (DI) water and 45 vol.% of 45S5 glass powder that was added in a stepwise manner between successive mixing steps in a centrifugal planetary mixer for around 20 min. Differential thermal analysis (DTA) results showed that CMC degradation occurred in two successive stages highlighted by two exothermic peaks at 225 °C and 350 °C. As a result, a de-binding treatment at 400 °C for 1 h prior to sintering was selected as optimal to yield full removal of the organic phase. The sintered scaffolds exhibited a compressive strength comparable to that of cancellous bone (2–13 MPa) and a porosity of 20 vol.% at the highest sintering temperature (1050 °C). A similar ink formulation [49] with 1.5 wt% CMC and 42 vol% 13–93 glass loading could also be extruded through a conical

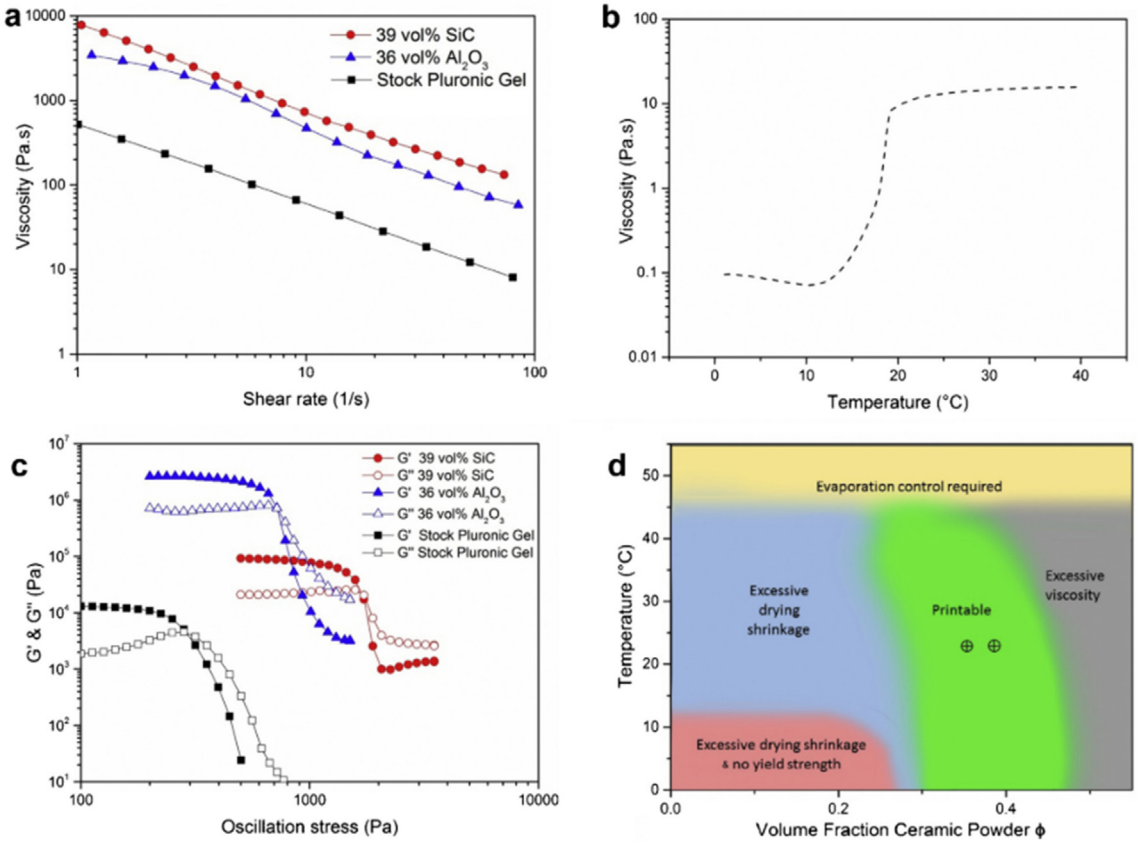

Figure 8. a) Flow ramps of Al_2O_3 and SiC inks compared to the stock gel. b) Viscosity temperature sweep of the F127 showing the reversible gelation between 10 and 20 °C. c) DMA of the hydrogel gel and SiC and Al_2O_3 inks at 1 Hz. (d) Estimated viability map of different inks printing at different temperatures incorporating the major limiting effects during printing adapted with permission from [66].

nozzle with an inner diameter of 410 μm, yielding a good powder dispersion and flowability. A successful implementation of CMC/glass-containing inks deposited by robocasting in reversible solid oxide cell applications has been reported by Lamnini et al [50]. Ink with 37 vol% of glass, exhibiting a viscosity of 2.6 × 104 Pa s and storage modulus as high as 1.4×10^5 Pa, was selected for printing on Crofer22APU steel substrate. Optimized de-binding and sintering stages enabled high-quality Crofer22APU/glass sealant joining with a reproducible thickness and good structural integrity.

Gel-embedded suspensions based on non-ionic thermosensitive hydrogel such as Pluronic F-127 are widely reported in the literature [42, 51]. Pluronic consists of the combination of polyethylene oxide and polypropylene oxide in a 2:1 ratio. Based on the temperature and water content, Pluronic presents either a hydrophobic or hydrophilic behaviour. Gelation of Pluronic F-127 is thermally reversible and induces the pseudoplastic properties. In this regard, bone tissue-engineering scaffolds with compressive strength of 6 MPa and Young's modulus of 340 MPa, which are comparable to human cancellous bone, were successfully prepared by Baino et al. [52] using robocasting and Pluronic F-127 as a multifunctional binder. Long stirring overnight of F-127 solution was performed in an ice bath to ensure F-127 dissolution and maintain adequate viscosity of the solution. Inks containing 35 vol.% of bioactive glass were printed to fabricate scaffold structures undergoing a three-step de-binding process (200, 400, and 500 °C for 30 min each) followed by a final sintering stage at 600 °C for 1 h.

In order to study the influence of defects (voids) on the fracture behaviour under uniaxial compression in the context of bone substitution, Laurent et al [53] prepared a scaffold from a combination of hydroxyapatite (HA, 20 vol%) and tricalcium phosphate (TCP, 80 vol%). The total solid loading of the ink was 30 vol%; 2 vol% of polymeric beads were added to the Pluronic solution to intentionally create artificial defects within the scaffold structure. A de-binding temperature of 550 °C for 2 h was fixed to remove the Pluronic beads and binder, while the sintering occurred at 1100 °C for 4 h. It was confirmed that the artificial defects led to important stress concentration and played a key role in crack initiation at the maximal principal stresses obtained by finite element modelling.

Calcium phosphate inks based on Pluronic F-127 were also developed by Santiago et al [54] using robocasting. Pluronic solution was mixed in a dual asymmetric centrifugal mixer first at 3500 rpm for 1 min and then at 3500 rpm for 5 min. Hydrothermal-immersion treatment of the printed calcium phosphate scaffolds was found to significantly reduce the hardening time to 30 min and yield compressive strengths comparable to trabecular bone. In another work, complex monolithic alumina ceramic parts with a high density of 97% and strength up to 230 MPa were successfully produced by Feilden et al. [42] using Pluronic F-127 hydrogel ink and robocasting. Specifically, two planetary mixing processes at 2000 rpm for 1 minute were followed by immediate cooling to 0 °C and stirring to maintain an adequate viscosity of Pluronic solution and break agglomerates due to the stepwise addition of 40 vol% Al_2O powder. De-binding was accomplished by heating the printed parts at 600 °C for 2 h in air followed by pressureless sintering at 1550 °C for 1 h in air. Eqtesadi et al. [55] have pioneered the fabrication of geometrically complex boron carbide (B_4C) components by combining robocasting and pressureless spark plasma sintering, eventually leading to ultra-fast and highly-efficient densification. Successful geometrically complex B_4C ceramic parts reached a density of 95% ± 3% at 2100 °C after sintering and high mechanical properties (hardness 27 GPa, compressive strength 1800 MPa).

Recently, Lakhdar et al. presented a detailed study on the influence of ceramic solid loading and Pluronic F-127 binder concentration on the rheological properties and printing resolution in the fabrication process

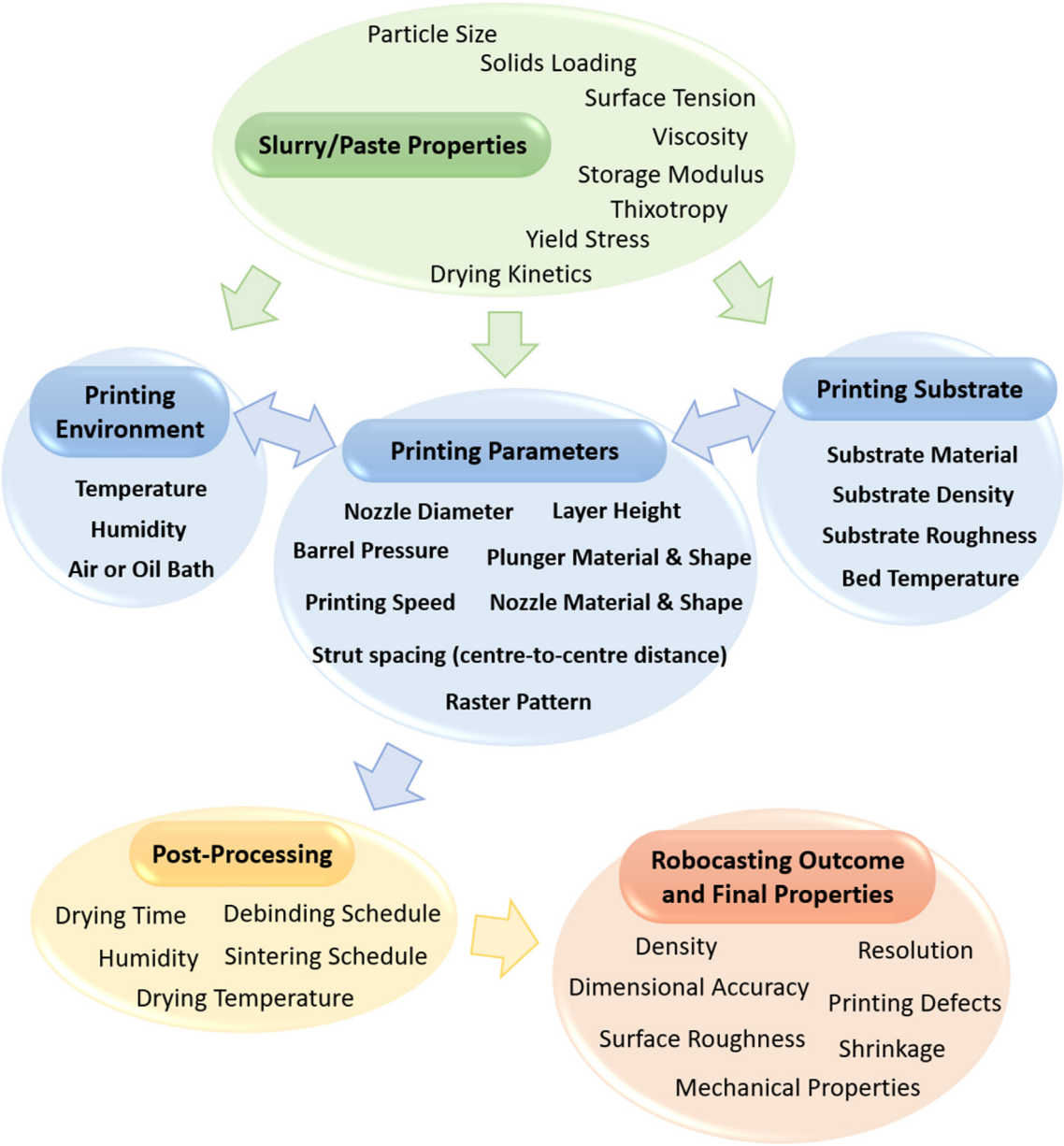

Figure 9. Map of the relationships between robocasting variables including the properties of the initial ceramic paste, the post-printing variables, and the final properties of printed ceramic samples.

of B_4C monoliths using robocasting and pressure-less sintering to produce fully-dense parts [56]. The inks were charged with B_4C ranging from 46 to 50 vol%. A dispersion agent of PEI was fully dissolved in DI water for at least 3 h, 1 wt% of stearic acid to regulate pH of B_4C pastes towards acidic values, while the Pluronic F-127 (10–17 wt%) promoted a thickening and stiffening effect. B_4C was progressively added in batch to the PEI/water solution and mechanically mixed in a planetary centrifugal mixer at 2000 rpm for 1 min, once at the beginning and then twice with a 15 s cool-off break. The addition of carbon-black (8 wt% relative to B_4C powder) served as a sintering aid to enhance both density and hardness. Pastes with the highest solid loading of 50 vol% displayed a too viscous behaviour that halted paste from being extruded. By contrast, the ink with 46 vol% solid loading oozed from nozzle tip regardless of the printing process due to too low stiffness and viscosity. The effect of Pluronic concentration was investigated as well: a low Pluronic concentration of 10 wt% led to a premature drying at the nozzle tip, which caused a clogging effect; thus, the solid loading and Pluronic concentrations were fixed in the range of 47–49 vol% and 15–17 wt%, respectively. The optimal ink containing 48 vol% B_4C and 17 wt% Pluronic led to a high density of 97 %.

Geometrically complex 3D structures of silicon carbide (SiC) were produced by robocasting using aqueous colloidal ink consisting of 44 vol % SiC, Al_2O_3, and Y_2O_3 particles in a dilute polymer solution of high-molecular weight polyethyleneimine (H-PEI), low-molecular weight PEI (L-PEI), methylcellulose, and ammonium polyacrylate (APA) [31]. The final products obtained by low-pressure spark plasma sintering (LPSPS) exhibited a solid density above 97% of theoretical density (TD) and a linear shrinkage of only ~22.8%. The same multi-additive system used for SiC in reference [31] allows printing other ceramics like silicon nitride (Si_3N_4) [57], aluminum nitride (AlN) [58] and robust architectured graphene/SiC [59].

Porous zirconia scaffolds for load-bearing bone implants were reliably produced by Gaddam et al. [60] using robocasting. Highly concentrated inks with 48 vol.% solid loading enabled to obtain porous zirconia scaffolds with strut density of 6.04 ± 0.06 g cm^{-3}, which was close to the theoretical density of YSZ ($\rho = 6.05$ g cm^{-3}). Besides, remarkably low

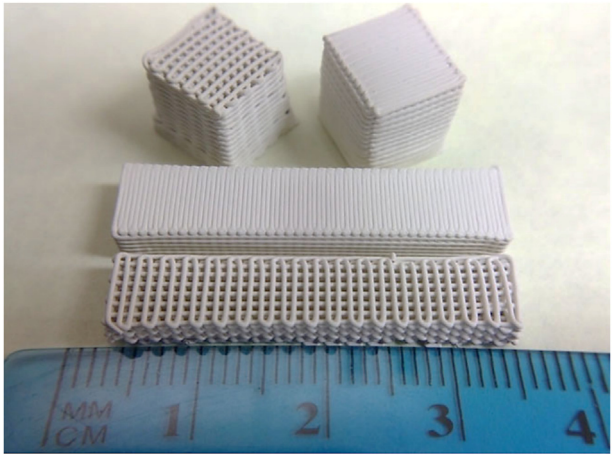

Figure 10. Optical photographs of Si_3N_4 green parts (cuboidal or beam geometries) with porous grid-like or solid architectures; adapted with permission from [69].

shrinkages of 19.18 ± 0.08% upon sintering at 1450 °C were reported and the scaffold exhibited a mean compressive strength of ~236 MPa and a Weibull modulus of 7.5, suggesting a good reliability of the fabrication process. For the same purpose, ceria-stabilized zirconia scaffolds with hierarchical porosity up to 85 vol% were fabricated by Tabard et al. [61] using robocasting. Different types of potato, wheat and rice starches were introduced, separately or combined, into the ink containing up to 36 vol % solid loading in order to tune the pore features. Specifically, three classes of pores were obtained, i.e., macroscopic pores (100 μm- 2 mm) controlled by the robocasting design, microscopic pores (2–70 μm) controlled by the addition of starches as pore formers in the ink, and sub-micronic pores (<200 nm) left behind by the partial sintering step. Crack formation induced by the drying effect was prevented in starch-containing scaffolds due to (i) gelling and swelling by water uptake that minimizes the evaporation speed and (ii) the higher permeability of starch-containing scaffolds to water. Silicone-based inks are quite attractive for the preparation of porous glass-ceramics scaffold. From this perspective, Elsayed et al. used particular inks based on MK silicone combined with inorganic fillers [46, 47]. The MK silicone successfully provided a double effect, by acting as a binder for inorganic powders and by offering most of the silica in the final ceramics, thereby serving as a preceramic polymer. Unlike conventional 'fugitive' binders, silicones bind fillers up to high temperatures and may be the dominant raw material for various silicates, especially in the case of polymers with 'high ceramic yield' (as an example, any gram of MK silicone yields up to 0.84 grams of amorphous silica, upon thermal decomposition in air). Wollastonite-diopside glass-ceramic scaffolds were obtained by using inks comprising MK silicone combined with oxide fillers ($CaCO_3$ and $Mg(OH)_2$) and glass particles. The MK powder was initially dissolved in isopropanol (IPA) and then mixed with fumed silica (FS), to control ink rheology. Glass powders were considered in order to determine some liquid phase upon firing (at 1100 °C), sealing the micro-cracks in the scaffold struts generated by the transformation of the silicone polymer. Interestingly, since the chemical formulation of the glass additive matched that of the product of silicone-filler interaction, the crystallization of the same glass offered additional wollastonite and diopside, without altering the relative balance [62]. Ball milling for 4 h at 400 rpm was performed for ink homogenization. A more radical approach involved an ink based on MK (and a minor amount of FS) and 'silica--defective glass', denoted as WB-15, to form wollastonite/Ca-borate scaffolds with compressive strength of 16.9 ± 1.8 MPa, which was comparable to bone tissue [63]. The final phase assemblage was found to depend on the reaction between MK-derived silica and glass. Compared to a glass with the same overall chemical formulation (WB), the MK/WB-15 mixture offered a superior control on the geometry of scaffolds, by preventing excessive viscous flow (MK, at the early stage of interaction, upon firing, led to a sort of rigid 'silica skeleton').

Table 1 summarizes the major ceramic ink compositions developed for robocasting as well as the post-printing heat treatment procedures designed for the intended applications. Generally, the de-binding process addressed to remove organic additives from the ink is carried out in single or multiple stages at relatively low temperatures in the range of 350–850 °C for (1 or 2 h per step). By contrast, in some works [55, 64] this stage has been skipped due to low binder concentration. In some medical (scaffolds for bone regeneration) or energy storage applications (batteries), the porosity of the sintered material is purposely introduced and can reach till 85 vol% [61]. However, the achievement of high densities (90–97% TD) is generally pursued to produce geometrically complex structures for industrial applications (abrasive tools, sandblasting nozzles) (see Figure 3a-d). These products are obtained by increasing the solid loading up to 50 vol% along with the use of SPS or SPSP sintering in argon or vacuum for 5 min [31, 55, 56]. Controlled blending and mixing of powders are usually done in optimised multistep mixing processes using a planetary centrifugal mixer.

3. Influence of particle features and solid loading on ink rheology

The physical features of powders have a vital effect on paste rheology for robocasting. Among others, particle size distribution and shape, powder density and volume fraction are the most significant factors [70,

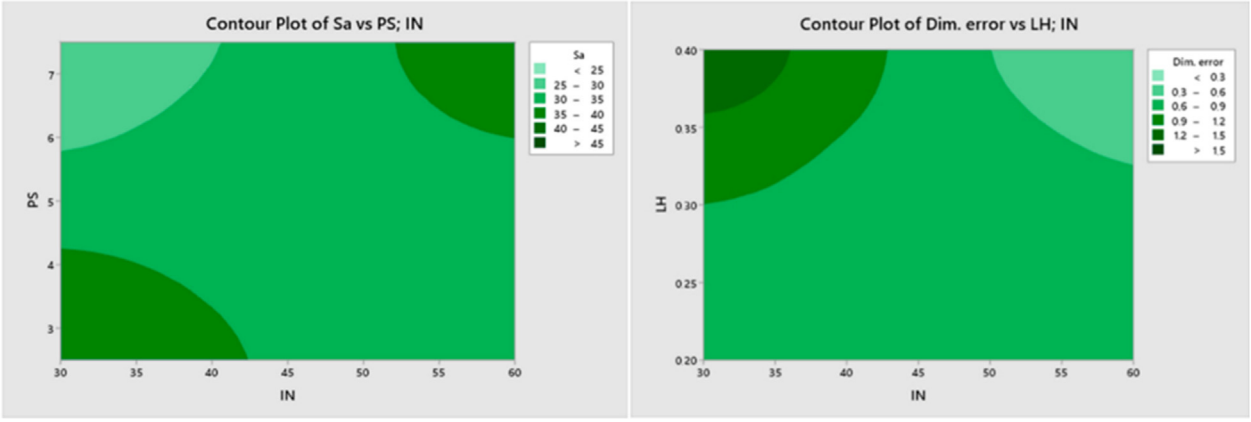

Figure 11. Contour plots of (left) mean arithmetical roughness Sa (μm) vs. infill (IN) and printing speed (PS), and (right) dimensional error (%) vs. infill (IN) and layer height (LH); adapted with permission from [95].

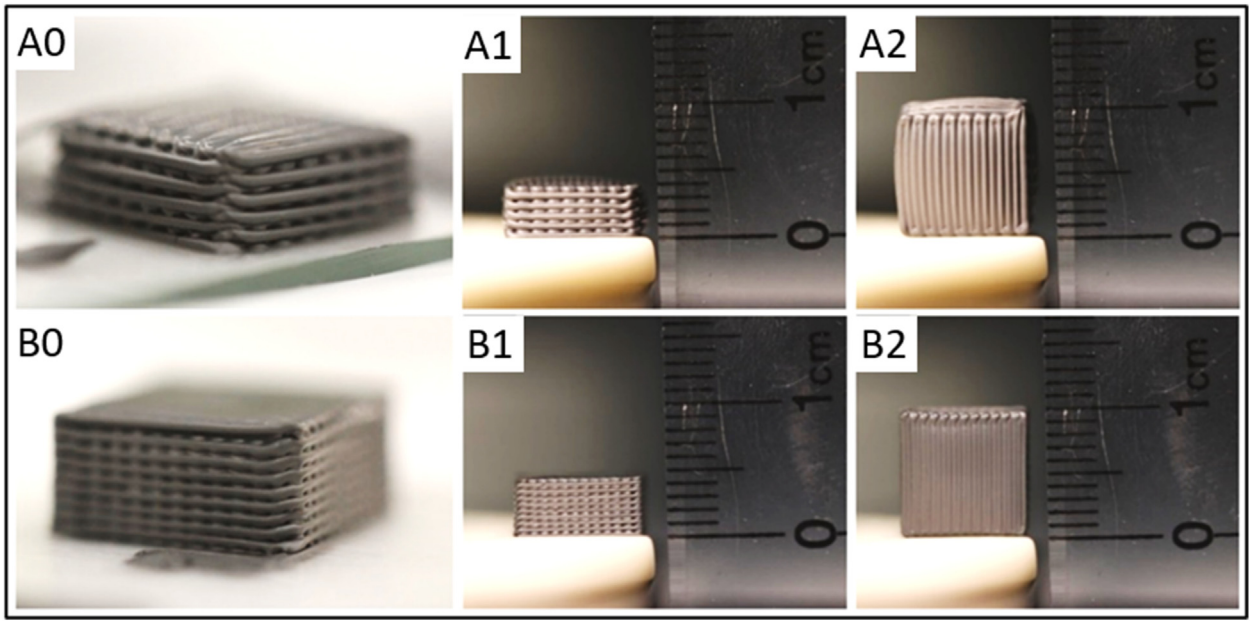

Figure 12. B_4C green parts produced using the 584 μm (A0-2) and 406 μm (B0-2) extrusion orifices; better resolution and shape retention were achieved with the finer extrusion nozzle. Printing parameters: 47 vol% B_4C paste, 80 psi (550 kPa) syringe pressure, 4 mm/s deposition speed, and 440 μm layer height (A); and 47 vol%, 30 psi (200 kPa), 4 mm/s, and 260 μm, respectively (B). Adapted with permission from [56].

71]. Thus, the control of the ink viscoelastic response requires as a first step a careful selection of powder features. Ceramic particles with various size and morphologies, such as sphere-like and platelet-like shapes, are presented in Figure 4 a/b and Figure 4 c respectively. Spherical particles are beneficial to increase the paste flowability due to the lower inter-particle interaction and friction compared to irregular and platelet-like particles. By contrast, the platelet-like particles with irregular edges particles tend to interlock with each other, thereby leading to cohesive behaviour and agglomeration even at low solid loading [72, 73, 74, 75]. The viscosity of pastes with irregular shape decreases if the applied shear conditions on the paste align the particles. In general, higher packing density yielding higher densities in final sintered parts is obtained with irregular particles [76, 77, 78]. In this context, Lorenz et al. [79] succeeded in developing printable pastes for robocasting containing both Al_2O_3 spheres and platelet-like powders with a bimodal size distribution of about ~0.5 and ~7 μm, respectively. The content of Al_2O_3 platelet powder ranged from 20 to 40 vol% per the total solid loading. It has been found that the total fraction of solid loading suitable for pastes preparation decreases slightly as the amount of platelets increases. Figure 5 a presents the amplitude sweep analysis of pastes containing Al_2O_3 platelet at various content of 20, 30, 40 vol% in relation to the total ceramic content of 51, 50, 45 vol%. The yield stress follows a tendency that is inversely proportional to the Al_2O_3 platelet content, thus confirming the main effect of platelet shape and content to tune the rheological properties of the pastes. In addition, the 20 and 30 vol% platelet-containing pastes were suitable for printing with nozzles of 0.5 mm and 1.5 mm diameter, while the 40 vol% Al_2O_3 platelet paste could only be extruded with a thicker nozzle of 1.5 mm in diameter, regardless of the total filling fraction. This was linked with the shear alignment behaviour of the platelets that occurred up to 30 vol% and eased the extrusion through a lower diameter. Thus, both powder geometry and total filling fraction should be taken into consideration while estimating the printability. Higher powder densities, on the other hand have been shown to enhance the packing due to the gravitational effects that governs particle surface adhesion forces [73].

The particle size distribution of the ceramic powder is another crucial factor determining the rheology of the paste and the density of the parts to be built. Variations in the particle size of the ceramic powder can result in orders of magnitude difference in viscosity and yield stress, typically between 0.2 and 200 μm. Finer powders are preferred for ink formulation as they allow better dispersion and sinterability, while large size particles have better flowability but are more prone to sediment. In fact, at a constant particle volume fraction, a narrow particle size distribution tends to increase the total surface area of the suspended particles by favouring a short interparticle distance which promotes strong particle-particle interactions [82, 83]. The formation of a typical chains and networks of touching particles with strong interactions lead to an increase in the viscosity and yield stress of the suspension [75, 84, 85].

Several studies have been performed to understand the influence of powder size, shape, and volume fraction on the rheological properties of colloidal inks.

The influence of particle size and content of $BaTiO_3$ platelet pastes containing lead-based perovskites has been the scope of a detailed work performed by Walton et al [83]. As presented by the amplitude sweep curve in Figure 5b the particle size has been grouped into small-sized platelets in the range of 5–20 μm and large-sized platelets in the range of 20–40 μm. The rheology of small and large $BaTiO_3$ platelets was investigated at concentrations of 1.4 vol% and 2.6 vol% from a total solid loading fraction of 28 vol%. Small platelet size (5 μm $< x <$ 20 μm) with concentrations of 1.4 vol% and 2.6 vol% exhibited $G' \sim$ 1000 kPa and yield stress ~1400 Pa.

By contrast, keeping the volume of platelets at 1.4 vol% and introducing larger platelets (20 μm $< x <$ 40 μm), G' significantly decreased to 60 kPa while the yield stress (σ_y) slightly increased to 1600 Pa. Similarly, introducing large platelets at the concentration of 2.6 vol% led to a slight increase of G' from 60 kPa to 180 kPa, while σ_y has been recorded at 1400 Pa. The influence of large anisotropic particles on paste rheology led to a drastic decrease of G' due to the relative size of the platelets compared to the equiaxed matrix particles, while the slight increase of σ_y can be linked to the alignment of platelets during shearing. In a similar work, Lorenz et al. [86] showed the influence of $BaTiO_3$ content on the overall paste rheological properties. The powder had a bimodal distribution with comparatively small size of $d_{50} = 1.2$ μm. A slight increase of the total solid loading from 50 vol% to 52 vol% resulted in a sharp upward of σ_y from 142 Pa to 694 Pa. A comparable trend was recognized with the G' and viscosity.

Yarahmadi et al. [87] aimed to evidence the particle size and content effect using 3Y-ZrO_2 and 8Y-ZrO_2 feedstocks on the paste flow and

Table 3. Printing parameters as key factors to predict the printing resolution and sintered density for different ceramic inks.

Ceramic feedstock	Solids loading (vol %)	Intended for dense monoliths (DM) or porous scaffolds (PS)	Orifice diameter *d* (μm)	Layer height (μm)	Printing speed (mm/s)	Rod/strut spacing, centre to centre (μm)	Printing strategy (raster pattern)	Printing substrate	Printing medium	Post-printing drying of green parts	Ref.
Al_2O_3	50	PS	500	-	10	-	Perpendicular layers	Smooth alumina	Oil bath, 20 ± 2 °C	~20 °C 24 h	[64]
B_4C	40	DM	410	356 (d/1.15) 328 (d/1.25)	20	342 (d/1.2) 820 μm (2d)	Parallel layers, hexagonal layup Tetragonal mesh	-	Ambient air	Oven drying 37 °C 48 h	[55]
Bioactive glass	35	PS	410	-	2	636	Perpendicular layers	Acetate sheets	Ambient air	Ambient air 48 h	[52]
Al_2O_3	40	DM	200	174 (d/1.15)	10	167 (d/1.2)	Parallel layers, hexagonal layup	Highly polished PTFE sheets	Air, 23 °C, 65–85 % humidity	Ambient air	[66]
B_4C	47–49	DM	406 584	260 440	4 4–5	-	Perpendicular layers	PTFE-coated glass slide	Ambient air	Room temperature 24 h	[56]
Si_3N_4	35	PS	410	-	10	410 910	Perpendicular layers	-	Ambient air	Room temperature 24 h	[69]
Bioactive glass	45	PS	410	287	10	820 (2d)	Perpendicular layers	-	Paraffin oil bath	Room temperature 24 h	[45]
HA/TCP 20:80 vol%/vol %	30	PS	150	-	20	300	Perpendicular layers	-	Oil bath	Air drying 3 days	[53]
SiC	0.44	DM	150–330	-	10	-	Perpendicular layers	Alumina	Paraffin oil bath	Air drying 23 °C	[31]
Si_2N_2O	21.17	PS	600	-	-	-	-	PTFE-coated glass slide	-	Oven drying	[68]
YSZ	48	PS	410	-	5	650 (estimated)	Perpendicular layers	YSZ	Paraffin oil bath	Room temperature	[60]
CEZ-12	36	PS	410	349	-	800	Perpendicular layers	PTFE- and coconut oil-coated smooth polymer sheet	Air, 23 °C, 98% RH	From 98%RH at 24 °C to 30%RH at 60 °C over four days	[61]
Al_2O_3	56	DM	400	480	3	-	Parallel layers	-	Air 55 °C	-	[100]
SiOC preceramic source - SiC powder	-	PS	410	360	10	1000	Perpendicular layers	-	Ambient air	Left overnight to cross-link and dry	[94]
YSZ (3YSZ)	18–30	PS	406	400	3	-	Perpendicular layers	-	Ambient air	-	[101]

viscosity. Inks based 3Y-ZrO_2 were investigated and compared to inks based 8Y–ZrO_2 to design new ceramic components. 3Y-ZrO_2 and 8Y-ZrO_2 powders had similar quasi-spherical morphology and bimodal shape distribution. The 8Y-ZrO_2 feedstock exhibited a finer size distribution with $D_{50} = 3.69$ μm, while 3Y-ZrO_2 feedstock had a coarse particles size distribution of $D_{50} = 8.03$ μm. Inks with the best viscoelastic properties corresponded to 73 and 70 wt% of 3Y-ZrO_2 and 8Y-ZrO_2 feedstocks, respectively. 8Y-ZrO_2 feedstock with fine particle size exhibited higher $\sigma_y = 2336$ Pa and $G' = (174 \pm 90) \times 10^{-3}$ Pa, compared to 3Y-ZrO_2 feedstock with coarse grain size ($\sigma_y = 1439$ Pa, $G' = (129 \pm 73) \times 10^{-3}$ Pa). It has been suggested that the viscosity variation is affected by yttrium content and grain size distribution.

It is generally recognized that the use of multi-modal powder size distributions can lead to better packing as fine particles tend to fill the voids between large particles, thereby promoting the achievement of printed parts with less interparticle voids and higher densities [76]. This "golden rule" is commonly followed in the processing of ceramic products by conventional methods, and can be rightly extended to 3D-printed materials, including sintered porous bodies [88]. In this regard, Mohammadi et al [80] investigated for the first time the potential and feasibility to prepare robocast dense zirconia parts with homogenous microstructure by using 3YSZ granules with multi-modal size distribution that spread from sub-micronic size to above 100 μm, with peaks located at 0.8 μm, 3.9 μm (minor peaks), 18.9 μm and 52.6 μm (major peaks). The wide granule size distribution improved the filling and packing properties as the small particles filled the voids between the larger ones [89]. Two powder feedstocks were used to investigate the influence of grain size on the ink rheology. The first was based on the coarse 3YSZ granules with uniform solid spheres and the second involved very fine particles with monomodal size distribution of 0.17 μm derived from the crushed granules. The optimal solid loading values with the best printing conditions were obtained at ~ 42 vol% and ~53 vol% for granules and fine particle-based suspensions, respectively. In fact, finer grains increased the total filling fraction of the paste and led to better rheological properties namely higher yield strength ($\sigma_y = 14.07$ kPa), storage modulus ($G' = 4 \times 10^6$ Pa) and more stable viscosity.

Although the viscosity of granule-based ink was comparatively lower than that of fine particle-based paste, the former showed a kind of instability characterized by fluctuated distribution at different shear rate as shown in Figure 5c. The viscosity instability due to large grains has been also reported elsewhere [90]. Further, the use of granule-based inks is found to be advantageous to ease the de-binding stage due to the large inter-granule spaces which enhance the final density of the sintered products.

In fact, the design of paste with high solid loading and relatively low viscosity remains a critical task to obtain high-quality printed ceramic parts through robocasting. The low viscosity facilitates paste extrusion and limits paste sedimentation or nozzles clogging, while high solid loading enhances material densification and reduces the drying effects that promotes shrinkage of the printed products. These aspects were studied by Guitián et al [91] who optimized ZnO-based inks for robocasting to manufacture cylindrical and square structures. The irregular powder shape of ZnO with monomodal size distribution (~0.7 μm) were investigated at solid loading in the range of (44–52 vol%). It has been confirmed that the initial viscosity at 0.1 s^{-1} shear rate increased gradually with ZnO content. However, from 48 vol% the initial viscosity rose sharply from 6.53 to 14.96 Pa s. Therefore, an ink with a ZnO content of 48 vol% was selected for the fabrication of self-supporting structures printed with a 200 μm nozzle.

Table 2 outlines the rheological properties of the previously discussed pastes-based ceramic feedstocks taking into account the effects of particle size distribution (bimodal, monomodal, multimodal), powder morphology, and solid loading. The explicit scheme shown in Figure 6 summarizes the key factors that influence the rheology of the pastes and the properties of the sintered part, depending on powder physical features.

4. Protocol to predict printing parameters for robocasting

Robocasting can be performed entirely without the need for any ultraviolet or laser radiation, making the process arguably simpler to operate and significantly cheaper than most - if not all - other ceramic additive manufacturing technologies. Nevertheless, the main difficulty of ceramic robocasting lies in the use of concentrated aqueous ceramic pastes of low organic content with fine-tuned rheological properties, to enable - on the one hand - controlled flow during extrusion through a fine orifice, and - on the other hand - shape retention upon selective deposition while avoiding the formation of drying cracks. Therefore, a good understanding of the relationships between the various robocasting printing parameters is essential to obtain ceramic parts with the desired physical characteristics and mechanical properties.

Robocasting counts a large number of processing, printing and post-printing variables that can all strongly affect the outcome of the process in terms of paste extrudability, dimensional accuracy, printing resolution, surface roughness, occurrence of defects, green density, and mechanical properties of ceramic samples.

As mentioned earlier, maximizing the ceramic solid content of aqueous pastes for robocasting is crucial to obtain 3D-printed ceramics with high density and minimal drying/sintering shrinkage to prevent crack formation. However, higher solid contents result in increased viscosity, yield stress σ_y and storage modulus G′, which could prevent paste extrusion and yield poor strut merging in the case of monolithic parts [56]. In the case of lattices and scaffolds, high solid loading leads to increased strut stiffness which is important for shape retention of free-standing and suspended struts [66]. It is therefore essential to formulate printing inks with the most appropriate rheological properties for robocasting operation to ensure printability while providing optimal shape retention and green density. Thus, for a given ink material system

Table 4. Qualitative evaluation of the relative importance of key feedstock, printing, and post-processing parameters on robocasting performance and final ceramic properties. Meaning the indexes: "-" low correlation, "+" low importance, "++" high importance, "+++" crucial factor.

Parameter	Throughput	Resolution	Density	Shrinkage	Surface Roughness	Mechanical strength
Feedstock Parameters						
Particle size	-	+	++	+	++	++
Solids loading	+	+	+++	+++	++	++
Printing Parameters						
Orifice diameter	+++	+++	++	+	+++	+
Printing speed	+++	+++	++	+	+	+
Layer height	+++	+++	++	+	++	+
Strut spacing	++	+	+++	++	++	++
Post-Processing Parameters						
Sintering temperature and/or pressure	+	-	+++	+++	-	+++

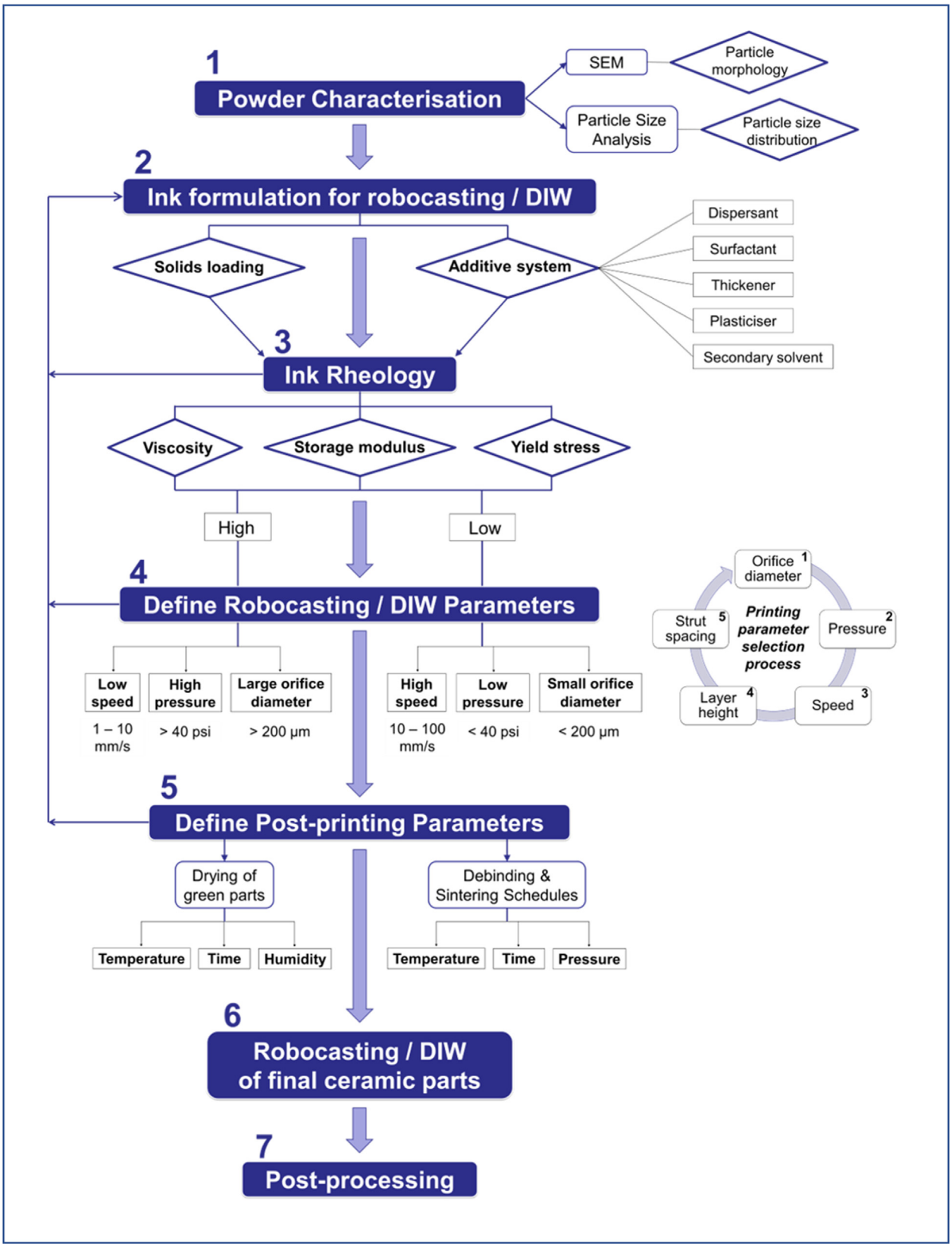

Figure 13. Robocasting protocol flowchart, from starting powder to final sintered and post-processed ceramic part.

there is a large number of possible formulations that would fit within the 'printability window', i.e. that have the desired set of rheological properties and enable ink extrusion with controlled selective deposition.

As shown in Figure 7a, colloidal particles in suspension are in a non-continuum state at low solid loadings with virtually no inter-particle interactions. As the particle volume fraction is increased, they then

form a weak particle network and finally a strong continuous network at high volume fractions. The printability window is typically defined as the range of values where both storage modulus G′ and yield stress σ_y (or flow stress σ_f) enable successful robocasting operation (Figure 7b) [15]. A low value of the yield stress σ_y, which is typically associated with low solid loadings, would result in poor control of the ceramic slurry during deposition and potential unwanted nozzle dripping due to the weak particle network. On the contrary, a highly concentrated paste cannot be extruded out of the printing orifice if σ_y is above the maximum extrusion pressure that can be applied by the robocasting system. Meanwhile, if the value of σ_y is suitable but the storage modulus G′ is too low due to low solid content, the ceramic paste filaments can be extruded but the struts would have a low stiffness resulting in poor shape retention. Although this can be beneficial to a certain extent to promote strut merging and lower surface roughness when monolithic parts are built [93], it is highly detrimental to the shape integrity of free-spanning filaments in structures with highly-complex shapes [39].

Flow properties of ceramic inks and gels can be approximated by the Herschel-Bulkley model [84]. Robocasting inks display a shear thinning behaviour characterised by an exponential decrease in viscosity as shear rate increases, as shown by the Pluronic-based SiC and Al_2O_3 slurries presented in Figure 8a. The gelation behaviour of the Pluronic gel is demonstrated in Figure 8b, displaying an increase in viscosity by two orders of magnitude at the gelation temperature of ~17.5 °C, making it ideal for storage at low temperature and printing at room temperature. Printable ceramic inks, as well as the Pluronic gel they are based on, exhibit the typical elastic behaviour at low stress followed by a yielding behaviour as the stress increases (Figure 8c), although storage and loss moduli, viscosity, and yield stress were all larger in the inks with ceramic powder.

The drying behaviour of the printing paste should also be considered when defining printability since the printing temperature strongly affects paste rheology, shrinkage, and crack formation in the green state. Therefore, a plot showing printing temperature against paste volume fraction also provides valuable information to narrow down the range of paste solid loadings and printing temperatures that can yield 'printable' ceramic inks (Figure 8d) [66]. This is where the optimisation of robocasting parameters to account for the specific rheological and drying behaviour of a given ceramic ink plays an essential role in enabling not only printability per se but also optimal printing outcome.

An exhaustive list of the possible robocasting variables including both the properties of the initial ceramic paste and the post-printing variables mapped against the final properties of printed ceramic samples that can be influenced is provided in Figure 9.

There is a deep interplay between all these processing and printing parameters and modifying anyone of them can have a significant impact on the robocasting outcome. For instance, increasing the solid loading of the paste typically results in higher paste viscosity and stiffness, which may be beneficial for shape retention upon deposition of extruded ceramic rods and for avoiding structural slumping, but it would likely also mean that printing speed needs to be reduced and/or extrusion pressure increased to account for the higher paste viscosity. Furthermore, changing the powder-to-solvent ratio may result in different drying kinetics which leads to the formation of printing defects and drying cracks. Higher solid loadings also tend to complicate extrudability by increasing the chance of nozzle clogging, which can result in having to increase the printing orifice diameter to prevent clogging; this in turn affects resolution, density and mechanical properties [56, 94].

The choice of printing parameters is greatly influenced by the intended geometry to be printed, namely either dense monolithic specimens or porous scaffolds (Figure 10). First, the direct effect on the inter-strut distance during deposition should be taken into account as dense parts require ceramic rods to merge together to prevent the formation of inter-strut porosity, while porous scaffolds need a user-defined spacing between rods to create designed macropores. Second, the medium in which the printing operation is performed also plays a role: in this regard, Feilden et al. [66] pointed out that while robocasting of porous scaffolds is often carried out in paraffin oil bath [31, 45, 53, 60, 64], it is not suitable for monolith manufacture as pockets of oil tend to get trapped in-between densely packed ceramic rods, thus leading to printing defects and unwanted porosity.

Buj-Corral et al. [95] investigated the role of robocasting printing parameters on the surface roughness and dimensional accuracy of the lateral walls of porous prismatic zirconia parts. The extrusion orifice diameter was 0.67 mm, and the ink formulation was 40 vol% of ZrO_2 (mean particle size of 40 μm) mixed with a 25 wt% Pluronic acid solution. The robocasting variables were infill, layer height, printing speed, extrusion multiplier, and bed temperature. Results showed that low infill (30%) along with low layer height (0.2 mm) and a printing speed of 7.5 mm/s yielded the lowest surface roughness, while higher infill (50%) combined with lower printing speed (2.5 mm/s) and high layer height (0.4 mm) were recommended to decrease the dimensional error.

Two-dimensional heat maps of the results are provided in Figure 11. The former set of parameters was also shown to provide the best overall result when trying to minimise both dimensional error and surface roughness at the same time. Furthermore, the higher printing speed had the added value of shortening the printing time and improving the resolution, while low infill also resulted in accelerated manufacturing and lower material use, which eventually improve production efficiency and lower cost. However, it is necessary to study the impact of these printing variables on more aspects than just the lateral walls of printed parts, in particular on mechanical properties and scalability.

Feilden et al. [66] also detailed the effects of several printing parameters on the final properties of monolithic Al_2O_3 and SiC samples. They pointed out the dramatic influence of the size of the extrusion tip on extrudability, resolution, dimensional accuracy, and surface roughness of printed ceramic parts. The use of larger extrusion tips resulted in lower dimensional accuracy and increased surface roughness, which could act as the source of cracks thereby reducing mechanical properties; on the contrary, fine nozzles required excessive syringe pressure beyond the machine capabilities to enable paste extrusion. They used a conical nozzle with a diameter d of 200 μm and determined empirically the most appropriate layer height and strut spacing to be $d/1.15$ and $d/1.2$, respectively, with hexagonal stacking of the filaments for increased packing density.

Lakhdar et al. [56] also showed that reducing the diameter of the extrusion orifice from 584 μm to 406 μm resulted in significantly higher dimensional accuracy, lower staircasing effect and higher green density when printing monolithic boron carbide samples.

The diameter of the printing nozzle is typically the first printing parameter that is set as it has a direct impact on the resolution of the process, which is in turn determined by the specifications of the final ceramic part in terms of geometry and application. A large extrusion orifice may result in significant staircasing effects, wall slumping and increasing sample deformation with layer count. Indeed, large ceramic struts are more prone to slumping because of their own weight and because they dry much faster at the surface than at their core due to their high volume-to-surface ratio.

Finer extruding tips enable the production of thinner, lighter struts of reduced volume-to-surface ratio that are stiffer, ultimately resulting in better shape retention and dimensional accuracy, as shown in Figure 12.

This is of course a well-known effect for robocasting in general [96, 97, 98], but reducing the orifice diameter is often challenging due to the faster drying kinetics and increased risk of clogging [55]. For a given ceramic ink, the size of the extrusion tip directly impacted on the range of syringe pressures which then had to be matched with the printing speed to prevent either 'under-pumping' or 'over-pumping', which were respectively described as the situations where the extruded struts are either finer or wider than intended upon deposition due to a mismatch between syringe pressure and travel speed. Optimizing these parameters is an essential and unavoidable step of the process to obtain consistent and reliable printing outcome.

The importance of preventing bubbles when loading the ceramic ink in the syringe was highlighted by several authors. Indeed, bubbles trapped in the ink can result in critical printing defects, in particular internal porosity and printing gaps [22, 49, 99].

The porosity of the printing substrate was found to directly impact the drying behaviour of printed samples as highly-porous substrates resulted in significant and instant warping of green parts due to faster drying kinetics [56]. The roughness of the printing substrate is another important parameter to consider, and most studies agree on the importance of using smooth, flat substrates made of or coated with a non-stick material, such as PTFE, to enable easy removal of printed parts [66, 68]. Table 3 provides an overview of the main printing parameters used in ceramic robocasting studies in the literature.

Therefore, this review aims to provide a comprehensive study of the relationships between feedstock properties, printing parameters, and post-processing parameters, to reveal the importance of carefully optimising these variables to avoid printing defects and maximise final ceramic properties, including density, surface roughness, and mechanical properties. Table 4 provides a qualitative evaluation of the impact of different ink features and processing parameters on the robocasting performance and the properties of the final ceramic body.

Figure 13 presents a general protocol for robocasting in the form of a flowchart with the practical sequence of the different steps to follow and characterisations to do for the development of suitable inks and the selection of printing parameters.

Finally, DIW technique offers an additional benefit of reduction in material waste and post-processing, and therefore this makes the DIW technology an economical and sustainable additive manufacturing process [102]. Post-deposition processes, such as drying, binder removal, and sintering, are required to give the printed part its final physic-mechanical characteristics. In addition, post-processing procedures, such as infiltration, can be used to further increase final mechanical properties. DIW technique of ceramic quite unsuitable to fabricate components with a decent surface quality without using finer nozzles, postprocess machining or a hybrid additive-subtractive manufacturing [14, 103, 104, 105].

5. Conclusions

Up to date, robocasting as a robust manufacturing technology achieved considerable progress in the fabrication of simple to complex and porous to dense ceramic structures. The so-obtained printed products are widely employed in the medical field (e.g., porous scaffolds for bone regeneration) or industrial applications (geometrically complex structures with high density ~90–97 % TD for abrasive tools, sand blasting nozzles etc.). Despite the substantial advancement that has been recently achieved in robocasting of ceramic materials, the scientific literature has reported the need to standardize the optimization of ink rheology designed for a specific application, and the related setting to control the printing parameters prior to the post-treatment stages. In fact, based on the application in purpose, the desired ink rheology may vary to a great extent. For example, relatively low yield stresses and storage modulus are necessary for glass ink formulations and 3D-bioprinting pastes to avoid opacity and cracking at post-processing stages. However, inks addressed to fulfil complex hierarchical 3D structures usually require stiff pastes to enable high printing resolutions. In fact, the rheological features of paste immediately after shearing are key to determine the mechanisms governing layer formation during printing. Among other factors, particle size distributions and shape, particle pure density, additive system and concentration, volume fraction of solid loading are major aspects influencing the rheological behaviour of the starting suspensions. A suitable paste for robocasting developed for an application, requires a quantified setting of all these factors besides adopting a relevant protocol to predict the suitable setting of the printing parameters. Hence, producing high dimensional resolution of the final printed parts. As a consequence, the ink formulation and optimization become quite complex and challenging. In this regard, the review focuses particularly on exploring the influence of particles physical features (size, shape, density) and volume fraction on controlling the ink rheology besides providing a guideline on predicting the printing parameters prior to post-treatment stage for a given ceramic ink. Several ink formulations and processing techniques were provided to facilitate the choice of a relevant additive system, its concentration, and multi-mixing steps. In this sense, the current review paper also underlines the beneficial use of carboxymethyl cellulose and Pluronic F-127 as multifunctional binders to easily tailor the pseudoplastic properties of inks for robocasting. However, further effort should be still extended to encompass a wider range of materials to promote the extensive use of robocasting over traditional synthesis methods based on well-defined printing and ink development protocols.

Declarations

Author contribution statement

All authors listed have significantly contributed to the development and the writing of this article.

Funding statement

This research did not receive any specific grant from funding agencies in the public, commercial, or not-for-profit sectors.

Data availability statement

This is a review article; the data are available in the original references.

Declaration of interests statement

The authors declare no conflict of interest.

Additional information

No additional information is available for this paper.

References

[1] M. Vaezi, H. Seitz, S. Yang, A review on 3D micro-additive manufacturing technologies, Int. J. Adv. Manuf. Technol. 67 (2013) 1721–1754.
[2] S. Guddati, A.S.K. Kiran, M. Leavy, S. Ramakrishna, Recent advancements in additive manufacturing technologies for porous material applications, Int. J. Adv. Manuf. Technol. 105 (2019) 193–215.
[3] N.W.S. Pinargote, A. Smirnov, N. Peretyagin, A. Seleznev, P. Peretyagin, Direct ink writing technology (3d printing) of graphene-based ceramic nanocomposites: a review, Nanomaterials 10 (2020) 1–48.
[4] Z. Chen, Z. Li, J. Li, C. Liu, C. Lao, Y. Fu, C. Liu, Y. Li, P. Wang, Y. He, 3D printing of ceramics: a review, J. Eur. Ceram. Soc. 39 (2019) 661–687.
[5] N. Travitzky, A. Bonet, B. Dermeik, T. Fey, I. Filbert-Demut, L. Schlier, T. Schlordt, P. Greil, Additive manufacturing of ceramic-based materials, Adv. Eng. Mater. 16 (2014) 729–754.
[6] A. Zocca, P. Colombo, C.M. Gomes, J. Günster, Additive manufacturing of ceramics: issues, potentialities, and opportunities, J. Am. Ceram. Soc. 98 (2015) 1983–2001.
[7] J.A. Lewis, J.E. Smay, J. Stuecker, J. Cesarano, Direct ink writing of three-dimensional ceramic structures, J. Am. Ceram. Soc. 89 (2006) 3599–3609.
[8] J.A. Lewis, Direct ink writing of 3D functional materials, Adv. Funct. Mater. 16 (2006) 2193–2204.
[9] C.F. Guo, M. Zhang, B. Bhandari, A comparative study between syringe-based and screw-based 3D food printers by computational simulation, Comput. Electron. Agric. 162 (2019) 397–404.
[10] S. Derakhshanfar, R. Mbeleck, K. Xu, X. Zhang, W. Zhong, M. Xing, 3D bioprinting for biomedical devices and tissue engineering: a review of recent trends and advances, Bioact. Mater. 3 (2018) 144–156.
[11] L. Hao, D. Tang, T. Sun, W. Xiong, Z. Feng, K.E. Evans, Y. Li, Direct ink writing of mineral materials: a review, Int. J. Precis. Eng. Manuf. - Green Technol. 8 (2021) 665–685.
[12] F. Zhang, Z. Li, M. Xu, S. Wang, N. Li, J. Yang, A review of 3D printed porous ceramics, J. Eur. Ceram. Soc. 42 (2022) 3351–3373.

[13] M. Methods, Processes A Comparison of Bioactive Glass Sca Ff Olds Fabricated by Robocasting from Powders Made by Sol – Gel and, 2020.
[14] Y. Lakhdar, C. Tuck, J. Binner, A. Terry, R. Goodridge, Additive manufacturing of advanced ceramic materials, Prog. Mater. Sci. 116 (2021), 100736.
[15] A. Corker, H.C.H. Ng, R.J. Poole, E. García-Tuñón, 3D printing with 2D colloids: designing rheology protocols to predict "printability" of soft-materials, Soft Matter 15 (2019) 1444–1456.
[16] X. Wan, L. Luo, Y. Liu, J. Leng, Direct ink writing based 4D printing of materials and their applications, Adv. Sci. 7 (2020) 1–29.
[17] E. Peng, D. Zhang, J. Ding, Ceramic robocasting: recent achievements, potential, and future developments, Adv. Mater. 30 (2018) 1–14.
[18] L. del-Mazo-Barbara, M.P. Ginebra, Rheological characterisation of ceramic inks for 3D direct ink writing: a review, J. Eur. Ceram. Soc. 41 (2021) 18–33.
[19] B.A.E.B. Ana, S.N. Isabel, M.M. Salvado, R.C. Pullar, J.M.F. Ferreira, Robocasting : Prediction of Ink Printability in Solgel Bioactive Glass, 2019, pp. 1608–1618.
[20] N.A. Dudukovic, L.L. Wong, D.T. Nguyen, J.F. Destino, T.D. Yee, F.J. Ryerson, T. Suratwala, E.B. Duoss, R. Dylla-Spears, Predicting nanoparticle suspension viscoelasticity for multimaterial 3D printing of silica-titania glass, ACS Appl. Nano Mater. 1 (2018) 4038–4044.
[21] E. García-Tuñón, E. Feilden, H. Zheng, E. D'Elia, A. Leong, E. Saiz, Graphene oxide: an all-in-one processing additive for 3D printing, ACS Appl. Mater. Interfaces 9 (2017) 32977–32989.
[22] P. Miranda, E. Saiz, K. Gryn, A.P. Tomsia, Sintering and robocasting of β-tricalcium phosphate scaffolds for orthopaedic applications, Acta Biomater. 2 (2006) 457–466.
[23] J. Cesarano III, Robocasting of Ceramics and Composites Using Fine Particle Suspensions, Univ. North Texas Libr, 1999. https://www.osti.gov/biblio/14157.
[24] I. Donderwinkel, J.C.M. Van Hest, N.R. Cameron, Bio-inks for 3D bioprinting: recent advances and future prospects, Polym. Chem. 8 (2017) 4451–4471.
[25] Z. Fu, P. Polfer, T. Kraft, A. Roosen, Correlation between anisotropic green microstructure of spherical-shaped alumina particles and their shrinkage behavior, J. Am. Ceram. Soc. 98 (2015) 3438–3444.
[26] G.W. Scherer, Theory of drying, J. Am. Ceram. Soc. 73 (1990) 3–14.
[27] J. Archez, N. Texier-Mandoki, X. Bourbon, J.F. Caron, S. Rossignol, Shaping of geopolymer composites by 3D printing, J. Build. Eng. 34 (2021), 101894.
[28] E. Feilden, D. Glymond, E. Saiz, L. Vandeperre, High temperature strength of an ultra high temperature ceramic produced by additive manufacturing, Ceram. Int. 45 (2019) 18210–18214.
[29] A. Nommeots-Nomm, P.D. Lee, J.R. Jones, Direct ink writing of highly bioactive glasses, J. Eur. Ceram. Soc. 38 (2018) 837–844.
[30] E. Feilden, C. Ferraro, Q. Zhang, E. García-Tuñón, E. D'Elia, F. Giuliani, L. Vandeperre, E. Saiz, 3D printing bioinspired ceramic composites, Sci. Rep. 7 (2017) 1–9.
[31] K. Cai, B. Román-Manso, J.E. Smay, J. Zhou, M.I. Osendi, M. Belmonte, P. Miranzo, Geometrically complex silicon carbide structures fabricated by robocasting, J. Am. Ceram. Soc. 95 (2012) 2660–2666.
[32] T.K. Sherwood, The drying of solids-III' mechanism of the drying of pulp and paper, Ind. Eng. Chemestry. 22 (2000) 132–136.
[33] E.R. Gilliland, T.K. Sherwood, The drying of solids. VI: diffusion equations for the period of constant drying rate, Ind. Eng. Chem. 25 (1933) 1134–1136.
[34] B.J. Briscoe, G. Lo Biundo, N. Özkan, Drying kinetics of water-based ceramic suspensions for tape casting, Ceram. Int. 24 (1998) 347–357.
[35] A. Zocca, G. Franchin, H. Elsayed, E. Gioffredi, E. Bernardo, P. Colombo, A. Bandyopadhyay, Direct ink writing of a preceramic polymer and fillers to produce hardystonite (Ca2ZnSi2O7) bioceramic scaffolds, J. Am. Ceram. Soc. 99 (2016) 1960–1967.
[36] A. Shahzad, I. Lazoglu, Direct ink writing (DIW) of structural and functional ceramics: recent achievements and future challenges, Compos. B Eng. 225 (2021) 109249.
[37] P. Bedarf, A. Dutto, M. Zanini, B. Dillenburger, Foam 3D printing for construction: a review of applications, materials, and processes, Autom. ConStruct. 130 (2021) 103861.
[38] K. Rane, M. Strano, A comprehensive review of extrusion-based additive manufacturing processes for rapid production of metallic and ceramic parts, Adv. Manuf. 7 (2019) 155–173.
[39] G.V. Franks, C. Tallon, A.R. Studart, M.L. Sesso, S. Leo, Colloidal processing: enabling complex shaped ceramics with unique multiscale structures, J. Am. Ceram. Soc. 100 (2017) 458–490.
[40] P. Thomas-Vielma, A. Cervera, B. Levenfeld, A. Várez, Production of alumina parts by powder injection molding with a binder system based on high density polyethylene, J. Eur. Ceram. Soc. 28 (2008) 763–771.
[41] R. Moreno, Colloidal processing of ceramic-ceramic and ceramic-metal composites, Process. Prop. Adv. Ceram. Compos. III. 225 (2011) 147–159.
[42] E. Feilden, M.I. Factory, L. Vandeperre, Robocasting of Structural Ceramic Parts with Hydrogel Inks, 2016.
[43] U. Scheithauer, T. Slawik, E. Schwarzer, H.J. Richter, T. Moritz, A. Michaelis, Additive manufacturing of metal-ceramic-composites by thermoplastic 3D-printing (3DTP), J. Ceram. Sci. Technol. 6 (2015) 125–132.
[44] S. Eqtesadi, A. Motealleh, P. Miranda, A. Lemos, A. Rebelo, J.M.F. Ferreira, A simple recipe for direct writing complex 45S5 Bioglass® 3D scaffolds, Mater. Lett. 93 (2013) 68–71.
[45] S. Eqtesadi, A. Motealleh, P. Miranda, A. Pajares, A. Lemos, J.M.F. Ferreira, Robocasting of 45S5 bioactive glass scaffolds for bone tissue engineering, J. Eur. Ceram. Soc. 34 (2014) 107–118.
[46] Q. Fu, E. Saiz, A.P. Tomsia, Direct ink writing of highly porous and strong glass scaffolds for load-bearing bone defects repair and regeneration, Acta Biomater. 7 (2011) 3547–3554.
[47] X. Liu, M.N. Rahaman, G.E. Hilmas, B.S. Bal, Mechanical properties of bioactive glass (13-93) scaffolds fabricated by robotic deposition for structural bone repair, Acta Biomater. 9 (2013) 7025–7034.
[48] F. Han, D. Xiong, Q. Wang, B. Shao, M. Chen, Thermal properties of carboxymethylcellulose and methyl methacrylate graft copolymers, J. Macromol. Sci., Part B: Phys. 52 (2013) 1242–1249.
[49] S. Eqtesadi, A. Motealleh, A. Pajares, P. Miranda, Effect of milling media on processing and performance of 13-93 bioactive glass scaffolds fabricated by robocasting, Ceram. Int. 41 (2015) 1379–1389.
[50] S. Lamnini, F. Baino, G. Montalbano, H. Javed, F. Smeacetto, Printability of carboxymethyl cellulose/glass-containing inks for robocasting deposition in reversible solid oxide cell applications, Mater. Lett. 318 (2022), 132239.
[51] V.G. Rocha, E. García-Tuñón, C. Botas, F. Markoulidis, E. Feilden, E. D'Elia, N. Ni, M. Shaffer, E. Saiz, Multimaterial 3D printing of graphene-based electrodes for electrochemical energy storage using thermoresponsive inks, ACS Appl. Mater. Interfaces 9 (2017) 37136–37145.
[52] F. Baino, J. Barberi, E. Fiume, G. Orlygsson, J. Massera, E. Verné, Robocasting of bioactive SiO2-P2O5-CaO-MgO-Na2O-K2O glass scaffolds, J. Healthc. Eng. 2019 (2019).
[53] C. Petit, S. Meille, E. Maire, L. Gremillard, J. Adrien, G.Y. Lau, A.P. Tomsia, Fracture behavior of robocast HA/β-TCP scaffolds studied by X-ray tomography and finite element modeling, J. Eur. Ceram. Soc. 37 (2017) 1735–1745.
[54] S. Raymond, Y. Maazouz, E.B. Montufar, R.A. Perez, B. González, J. Konka, J. Kaiser, M.P. Ginebra, Accelerated hardening of nanotextured 3D-plotted self-setting calcium phosphate inks, Acta Biomater. 75 (2018) 451–462.
[55] S. Eqtesadi, A. Motealleh, F.H. Perera, P. Miranda, A. Pajares, R. Wendelbo, F. Guiberteau, A.L. Ortiz, Fabricating geometrically-complex B4C ceramic components by robocasting and pressureless spark plasma sintering, Scripta Mater. 145 (2018) 14–18.
[56] Y. Lakhdar, C. Tuck, A. Terry, C. Spadaccini, R. Goodridge, Direct ink writing of boron carbide monoliths, J. Eur. Ceram. Soc. 41 (2021) 76–92.
[57] M.A. Sainz, S. Serena, M. Belmonte, P. Miranzo, M.I. Osendi, Protein adsorption and in vitro behavior of additively manufactured 3D-silicon nitride scaffolds intended for bone tissue engineering, Mater. Sci. Eng. C. 115 (2020), 110734.
[58] M. Belmonte, G. Lopez-Navarrete, M.I. Osendi, P. Miranzo, Heat dissipation in 3D printed cellular aluminum nitride structures, J. Eur. Ceram. Soc. 41 (2021) 2407–2414.
[59] B. Román-Manso, F.M. Figueiredo, B. Achiaga, R. Barea, D. Pérez-Coll, A. Morelos-Gómez, M. Terrones, M.I. Osendi, M. Belmonte, P. Miranzo, Electrically functional 3D-architectured graphene/SiC composites, Carbon N. Y. 100 (2016) 318–328.
[60] A. Gaddam, D.S. Brazete, A.S. Neto, B. Nan, H.R. Fernandes, J.M.F. Ferreira, Robocasting and surface functionalization with highly bioactive glass of ZrO2 scaffolds for load bearing applications, J. Am. Ceram. Soc. (2021) 1–12.
[61] L. Tabard, V. Garnier, E. Prud'Homme, E.J. Courtial, S. Meille, J. Adrien, Y. Jorand, L. Gremillard, Robocasting of highly porous ceramics scaffolds with hierarchized porosity, Addit. Manuf. 38 (2021), 101776.
[62] H. Elsayed, P. Colombo, E. Bernardo, Direct ink writing of wollastonite-diopside glass-ceramic scaffolds from a silicone resin and engineered fillers, J. Eur. Ceram. Soc. 37 (2017) 4187–4195.
[63] H. Elsayed, M. Picicco, A. Dasan, J. Kraxner, D. Galusek, E. Bernardo, Glass powders and reactive silicone binder : interactions and application to additive manufacturing of bioactive glass-ceramic sca ff olds, Ceram. Int. 45 (2019) 13740–13746.
[64] Z. Fu, M. Freihart, L. Wahl, T. Fey, P. Greil, N. Travitzky, Micro- and macroscopic design of alumina ceramics by robocasting, J. Eur. Ceram. Soc. 37 (2017) 3115–3124.
[65] H. Jin, D. Jia, Z. Yang, Y. Zhou, Direct ink writing of Si 2 N 2 O porous ceramic strengthened by directional β-, Ceram. Int. 46 (2020) 15709–15713.
[66] E. Feilden, E.G.T. Blanca, F. Giuliani, E. Saiz, L. Vandeperre, Robocasting of structural ceramic parts with hydrogel inks, J. Eur. Ceram. Soc. 36 (2016) 2525–2533.
[67] E. Ozkol, Rheological characterization of aqueous 3Y-TZP inks optimized for direct thermal ink-jet printing of ceramic components, ϵ 1130 (2013) 1124–1130.
[68] H. Jin, Z. Yang, D. Cai, D. Jia, Y. Zhou, 3D printing of porous Si2N2O ceramics based on strengthened green bodies fabricated via strong colloidal gel, Mater. Des. 185 (2020), 108220.
[69] S. Zhao, W. Xiao, M.N. Rahaman, D. O'Brien, J.W. Seitz-Sampson, B. Sonny Bal, Robocasting of silicon nitride with controllable shape and architecture for biomedical applications, Int. J. Appl. Ceram. Technol. 14 (2017) 117–127.
[70] J. Zhang, N. Amini, D.A.V. Morton, K.P. Hapgood, 3D printing with particles as feedstock materials, Adv. Powder Technol. 32 (2021) 3324–3345.
[71] A. Shahzad, I. Lazoglu, Direct ink writing (DIW) of structural and functional ceramics: recent achievements and future challenges, Compos. B Eng. 225 (2021) 109249.
[72] I. Gibson, D. Rosen, Additive Manufacturing Technologies, third ed., Springer Nature Switzerland, 2021.
[73] P. Shakor, S. Nejadi, G. Paul, J. Sanjayan, Dimensional accuracy, flowability, wettability, and porosity in inkjet 3DP for gypsum and cement mortar materials, Autom. ConStruct. 110 (2020), 102964.
[74] G. Lumay, F. Boschini, K. Traina, S. Bontempi, J.C. Remy, R. Cloots, N. Vandewalle, Measuring the flowing properties of powders and grains, Powder Technol. 224 (2012) 19–27.

[75] W. Pabst, E. Gregorová, C. Berthold, Particle shape and suspension rheology of short-fiber systems, J. Eur. Ceram. Soc. 26 (2006) 149–160.
[76] W. Du, X. Ren, C. Ma, Z. Pei, Binder jetting additive manufacturing of ceramics: a literature review, ASME Int. Mech. Eng. Congr. Expo. Proc. 14 (2017) 1–12.
[77] R. Gildenhaar, C. Knabe, C. Gomes, U. Linow, A. Houshmand, G. Berger, Calcium alkaline phosphate scaffolds for bone regeneration 3Dfabricated by additive manufacturing, Key Eng. Mater. 493–494 (2012) 849–854.
[78] J. Suwanprateeb, R. Sanngam, T. Panyathanmaporn, Influence of raw powder preparation routes on properties of hydroxyapatite fabricated by 3D printing technique, Mater. Sci. Eng. C. 30 (2010) 610–617.
[79] M. Lorenz, B. Dietemann, L. Wahl, C. Bierwisch, T. Kraft, H. Kruggel-emden, N. Travitzky, Journal of the European Ceramic Society Influence of platelet content on the fabrication of colloidal gels for robocasting : experimental analysis and numerical simulation, J. Eur. Ceram. Soc. 40 (2020) 811–825.
[80] M. Mohammadi, G. Becker, S. Diener, J. Tulliani, N. Katsikis, P. Palmero, Robocasting of dense zirconia parts using commercial yttria-stabilized zirconia granules and ultrafine particles . Paste preparation , printing , mechanical properties, Ceram. Int. 48 (2022) 1936–1946.
[81] L. Wahl, M. Weichelt, P. Goik, S. Schmiedeke, N. Travitzky, Robocasting of reaction bonded silicon carbide/silicon carbide platelet composites, Ceram. Int. 47 (2021) 9736–9744.
[82] Z. Zhou, M.J. Solomon, P.J. Scales, D.V. Boger, The yield stress of concentrated flocculated suspensions of size distributed particles, J. Rheol. 43 (1999) 651–671.
[83] R.L. Walton, M.A. Fanton, R.J.M. Jr, Dispersion and Rheology for Direct Writing lead-based Piezoelectric Ceramic Pastes with Anisotropic Template Particles, 2020, pp. 6157–6168.
[84] W.H. Herschel, R. Bulkley, The rheology of suspensions of solid particles, Proc. R. Soc. 39 (1926) 291–300.
[85] I. Santamaría-Holek, C.I. Mendoza, The rheology of concentrated suspensions of arbitrarily-shaped particles, J. Colloid Interface Sci. 346 (2010) 118–126.
[86] M. Lorenz, A. Martin, K.G. Webber, N. Travitzky, Electromechanical Properties of Robocasted Barium Titanate Ceramics, 2020.
[87] M. Yarahmadi, P. Barcelona, G. Fargas, E. Xuriguera, J.J. Roa, Optimization of the ceramic ink used in Direct Ink Writing through rheological properties characterization of zirconia-based ceramic materials, Ceram. Int. (2021) 2–8.
[88] F. Baino, E. Fiume, J. Barberi, S. Kargozar, J. Marchi, J. Massera, E. Verné, Processing methods for making porous bioactive glass-based scaffolds—a state-of-the-art review, Int. J. Appl. Ceram. Technol. 16 (2019) 1762–1796.
[89] L.C. Hwa, S. Rajoo, A.M. Noor, N. Ahmad, M.B. Uday, Recent advances in 3D printing of porous ceramics: a review, Curr. Opin. Solid State Mater. Sci. 21 (2017) 323–347.
[90] S.W. Jeong, Shear rate-dependent rheological properties of mine tailings: determination of dynamic and static yield stresses, Appl. Sci. 9 (2019).
[91] C.R. Tubío, F. Guitián, A. Gil, Journal of the European ceramic society fabrication of ZnO periodic structures by 3D printing, J. Eur. Ceram. Soc. 36 (2016) 3409–3415.
[92] J. Baltazar, M. Fellipe, R. Pais, C. Santos, Reactive Sintering of Al2O3–Y3Al5O12 Ceramic Composites Obtained by Direct Ink Writing, 2022, pp. 1–12.
[93] W. Rowlands, B. Vaidhyanathan, Additive manufacturing of barium titanate based ceramic heaters with positive temperature coefficient of resistance (PTCR), J. Eur. Ceram. Soc. 39 (2019) 3475–3483.
[94] G. Franchin, L. Wahl, P. Colombo, Direct ink writing of ceramic matrix composite structures, J. Am. Ceram. Soc. 100 (2017) 4397–4401.
[95] I. Buj-Corral, A. Domínguez-Fernández, A. Gómez-Gejo, Effect of printing parameters on dimensional error and surface roughness obtained in direct ink writing (DIW) processes, Materials 13 (2020).
[96] E. Peng, D. Zhang, J. Ding, Ceramic Robocasting : Recent Achievements , Potential , and Future Developments, 2018.
[97] J. Cesarano, A review of robocasting technology, Mater. Res. Soc. Symp. Proc. 542 (1999) 133–139.
[98] S.L. Morissette, J.A. Lewis, J. Cesarano, D.B. Dimos, T. Baer, Solid freeform fabrication of aqueous alumina-poly(vinyl alcohol) gelcasting suspensions, J. Am. Ceram. Soc. 83 (2000) 2409–2416.
[99] B.A.E. Ben-Arfa, R.C. Pullar, A comparison of bioactive glass scaffolds fabricated by robocasting from powders made by sol–gel and melt-quenching methods, Processes 8 (2020) 615.
[100] L. Yang, X. Zeng, A. Ditta, B. Feng, L. Su, Y. Zhang, Preliminary 3D printing of large inclined-shaped alumina ceramic parts by direct ink writing, J. Adv. Ceram. 9 (2020) 312–319.
[101] A.L. Troksa, H.V. Eshelman, S. Chandrasekaran, N. Rodriguez, S. Ruelas, E.B. Duoss, J.P. Kelly, M.R. Cerón, P.G. Campbell, 3D-printed nanoporous ceramics: tunable feedstock for direct ink write and projection microstereolithography, Mater. Des. 198 (2021), 109337.
[102] M.A.S.R. Saadi, A. Maguire, N.T. Pottackal, M.S.H. Thakur, M.M. Ikram, A.J. Hart, P.M. Ajayan, M.M. Rahman, Direct ink writing: a 3D printing technology for diverse materials, Adv. Mater. 2108855 (2022) 1–57.
[103] J. Hinton, M. Mirgkizoudi, A. Campos-Zatarain, D. Flynn, R.A. Harris, R.W. Kay, Digitally-driven hybrid manufacture of ceramic thick-film substrates, 2018 7th electron, Syst. Technol. Conf. ESTC 2018 - Proc (2018) 1–5.
[104] J. Hinton, D. Basu, D.F. Flynn, R.A. Harris, R.W. Kay, A digitally-driven Hybrid Manufacturing process for the flexible production of engineering ceramic components, Solid Free, in: Fabr. 2018 Proc. 29th Annu. Int. Solid Free. Fabr. Symp. - an Addit. Manuf. Conf. SFF 2018, 2020, pp. 388–397.
[105] S.S. Ramirez Caballero, H. Elsayed, S. Tadier, A. Montembault, E. Maire, L. David, T. Delair, P. Colombo, L. Grémillard, Fabrication and characterization of hardystonite-chitosan biocomposite scaffolds, Ceram. Int. 45 (2019) 8804–8814.